University of Brasília – UnB

Faculty of Gama

Postgraduate Program in Integrity of Materials Engineering

Information theory applied to numerical simulations of tokamak plasmas in a low-to-high confinement transition

Sarah Gomes da Silva Paes da Costa

Advisor: Prof. Dr. Rodrigo Andrés Miranda Cerda

University of Brasília – UnB

Faculty of Gama

Information theory applied to numerical simulations of tokamak plasmas in a low-to-high confinement transition

Sarah Gomes da Silva Paes da Costa

Advisor: Prof. Dr. Rodrigo Andrés Miranda Cerda

Master Thesis in Integrity of Materials Engineering Issue: 108A/2024

Brasília/DF, January 2024

University of Brasília – UnB
Faculty of Gama
Postgraduate Program in Integrity of Materials Engineering

Information theory applied to numerical simulations of tokamak plasmas in a low-to-high confinement transition

Sarah Gomes da Silva Paes da Costa

Master's thesis submitted to the postgraduate program in Integrity of Materials Engineering at University of Brasilia, as part of the requirements for obtaining a master's degree.

Approved by:

Prof. Dr. Rodrigo Andrés Miranda Cerda
Advisorr

Dr. Ronni Geraldo Gomes de Amorim
Examiner - FGA/UnB

Dr. Iberê Luiz Caldas
Examiner - IF/USP

Relatório (ata) de defesa de dissertação assinado eletronicamente pela banca avaliadora, via Sistema Eletrônico de Informações - SEI, documento 10704260, processo 23106.129955/2023-60.

Brasília/DF, January 2024

Catalographic Card

Costa, S. G. S. P.
Information theory applied to numerical simulations of tokamak plasmas
in a low-to-high confinement transition
[Distrito Federal], 2024.
53p., 210 × 297 mm (FGA/UnB Gama, Master in Integrity of Materials Engineering, 2024).
Master Thesis - University de Brasília.
Faculdade do Gama

1. Nuclear Fusion	2. Plasmas
3. Turbulence	4. Complexity
I. ENC/FGA/UnB.	II. Title (series)

Reference

Costa, S. G. S. P. (2024). Information theory applied to numerical simulations of tokamak plasmas in a low-to-high confinement transition. Master's Thesis in Integrity of Engineering Materials, Publication 108A/2024, Postgraduate Program, Faculty of Gama, University of Brasília, Brasília, DF, 53p.

s.gspcosta@gmail.com

Brasília, DF – Brazil

Acknowledgements

Gostaria de agradecer primeiramente a Deus e à mãe santíssima por cuidar de cada momento até aqui. Aos meus pais, Rosana e Geová por todo suporte, apoio, carinho e companheirismo com que me criaram, não posso fugir ao clichê de dizer que as palavras não exprimem tamanha gratidão e afeto que eu sinto por vocês, não chegaria em lugar algum se não fosse vocês.

Gostaria de agradecer também a minha família, de modo geral, por todo o carinho e apoio que mesmo à distância sempre demostraram, cada um à sua maneira. Gostaria de agradecer também ao Mateus Farias e a Giovanna Mayer por todo carinho e paciência nesse período de extrema ansiedade e agitação, o apoio irrestrito de todos foi fundamental pra essa conquista.

Presto também aqui meus sinceros agradecimentos aos meus amigos de jornada e companheiros de laboratório, em especial a Ana Luiza Piragibe, Helbert Júnior, William Wenner, Júlio Cesar, Laura Pires, Renan Almeida e tantos outros que fizeram o ambiente de pesquisa mais leve e tornaram a rotina mais agradável, além de todo aprendizado proporcionado, cada qual imbuído em um universo de saberes sempre dispostos a compartilhar, discutir e debater.

Agradeço imensamente aos professores, José Leonardo, Alexandre Martins, Ronni Amorim e em especial ao Professor Rodrigo Miranda pela paciência que tiveram para comigo e por todos os ensinamentos compartilhados, foi um privilégio trabalhar próximo a pessoas tão enriquecedoras e com tanto a compartilhar.

Agradeço à Fundação Coordenação de Aperfeiçoamento de Pessoal de Nível Superior - CAPES, pelo auxílio financeiro, crucial para o densenvolvimento do presente trabalho.

Resumo
Teoria da informação aplicada à simulação numérica de plasmas de tokamaks na transição do baixo para o alto confinamento

A turbulência exerce influência significativa sobre o transporte radial na região de borda dos plasmas no interior de tokamak, um fator crítico no confinamento magnético para experimentos de fusão. Apesar do seu impacto substancial, a compreensão da turbulência neste contexto permanece limitada. Estruturas coerentes são fundamentais no domínio do transporte turbulento dentro de plasmas de fusão. A entropia e a complexidade, derivadas da teoria da informação, servem como uma ferramenta valiosa para quantificar o nível de ordem ou desordem em plasmas turbulentos. Notavelmente, essas estruturas coerentes contribuem para a observação de baixos valores de entropia espectral em dados obtidos de plasmas espaciais e simulações numéricas de turbulência magnetohidrodinâmica.

Nesta análise, nos concentramos em simulações numéricas bidimensionais das equações modificadas de Hasegawa-Wakatani, que fornecem um modelo não linear simplificado para turbulência de ondas de deriva resistivas eletrostáticas em plasmas, construímos um diagrama de bifurcação que ilustra a transição de um regime turbulento para um dominado por fluxos zonais, suprimindo efetivamente a turbulência. Para avaliar o nível de ordem ou desordem espacial durante esta transição, calculamos o índice de complexidade-entropia de Jensen-Shannon da velocidade, derivado do potencial eletrostático. Este índice usa a potência normalizada dos coeficientes de shearlet como distribuição de probabilidade. As nossas descobertas revelam que o regime turbulento apresenta um maior grau de entropia e um menor grau de complexidade, contrastando com o regime dominado por fluxos zonais caracterizados por valores de entropia mais baixos e um maior grau de complexidade. Esses resultados têm potencial para avançar nossa compreensão de processos não lineares na turbulência de ondas de deriva em plasmas de fusão.

Palavras-chave: Plasma, teoria da informação, dinâmica não-linear, turbulência.

Abstract

Turbulence exerts significant influence over radial transport in the edge region of tokamak plasmas, and is a critical factor in magnetic confinement for fusion experiments. Despite its substantial impact, our understanding of turbulence in this context remains limited. Coherent structures are fundamental in the realm of turbulent transport within fusion plasmas. Entropy and complexity, derived from information theory, serves as a valuable tool to quantify the level of order or disorder in turbulent plasmas. Notably, these coherent structures contribute to the observation of low spectral entropy values in data obtained from space plasmas and numerical simulations of magnetohydrodynamic turbulence.

In this analysis, we focus on two-dimensional numerical simulations of the modified Hasegawa-Wakatani equations, which provide a simplified nonlinear model for electrostatic resistive drift-wave turbulence in plasmas. We construct a bifurcation diagram illustrating the transition from a turbulent regime to one dominated by zonal flows, effectively suppressing turbulence. The degree of spatial order or disorder during this transition is obtained by computing the Jensen-Shannon complexity-entropy index of the velocity, derived from the electrostatic potential. This index uses the normalized power of shearlet coefficients as a probability distribution. Our findings reveal that the turbulent regime exhibits a higher degree of entropy and a lower degree of complexity, contrasting with the regime dominated by zonal flows characterized by lower entropy values and a higher degree of complexity. These results hold the potential to advance our understanding of nonlinear processes within drift-wave turbulence in fusion plasmas.

Keywords: Plasma, information theory, nonlinear dynamics, turbulence.

Contents

List of Tables

List of Figures

List of Nomenclatures and Abbreviations

L-H low-to-high

ITER International Thermonuclear Experimental Reactor

H high-confinement

L low-confinement

LCFS last closed (magnetic) flux surfac

SOL Scrape-Off Laye

HW Hasegawa-Wakatani

MRA multiresolution analysis

FFST fast finite discrete shearlet transfor

C-H complexity-entropy

FFTW Fastest Fourier Transform in the West

MIT Massachusetts Institute of Technology

1 Introduction

Thermonuclear fusion refers to a reaction that commonly occurs in stars, such as the Sun, and is regarded as a clean and safe solution to the growing energy demand as the global population evolves and finite resources such as fossil fuels are depleted (Dewhurst, 2010). In this reaction, the nuclei fuse together, releasing energy. For this to occur an electrostatic barrier must be overcome, due to the integration of attractive nuclear forces with the positively charged nuclei, thus causing mutual electrostatic repulsion. The nuclear fuel is heated to high temperatures and completely ionized. The resulting plasma can be then confined by means of a magnetic field.

Maintaining the confinement of fusion plasmas is a major engineering challenge. A significant experimental breakthrough in the field of nuclear fusion research involved the detection of a low-to-high (L-H) transition of plasma confinement (Wagner et al., 1982). This transition markedly diminishes particle and energy losses from the core of magnetically confined plasma, thereby enhancing the prospects for successful nuclear fusion. Subsequently, L-H transitions have become commonplace observations in numerous contemporary tokamaks and stellarators. The designs of advanced facilities such as International Thermonuclear Experimental Reactor (ITER) place significant importance on achieving H-mode operation, largely influenced by these findings (Pushkarev, 2013a).

One of the explanations the L-H transition involves the suppression of turbulence through $\vec{E} \times \vec{B}$ flow shearing. This suppression effect can be attributed to mean $\vec{E} \times \vec{B}$ flows and/or to zonal flows (Burrell, 1997). The theoretical characterization of the L-H transition and nonlinear turbulent states in fusion devices is a considerable challenge since this complexity arises from the multitude of crucial physical parameters, scales of motion and intricate magnetic field geometries (Krommes, 2012).

In the pursuit of enhanced plasma confinement, a profound understanding of the low-to-high (L-H) confinement transition holds pivotal importance in the control of plasma within fusion experiments. This transition is crucial as it elevates plasma confinement by mitigating the effects of anomalous or turbulent plasma particles and heat fluxes. Notably, the emergence zonal flows plays a fundamental role in achieving high-confinement regimes. These flows effectively reduce anomalous transport by absorbing energy from drift waves and organizing eddies, thereby mediating turbulent transport. (Diamond et al., 2005; Numata et al., 2007).

By utilizing a simplified model to describe turbulence in tokamak plasmas, we can understand the L-H confinement transition as an outcome of the interaction among three energy

subsystems: the kinetic energy associated with turbulence, shear flow, and potential energy resulting from density or pressure gradients (Numata et al., 2007). This transition involve processes such as turbulence generation through drift waves, destabilization, and the self-organization of zonal flows, collectively leading to instabilities that represent a bifurcation of the equilibrium solution. These instabilities can be categorized into primary instabilities originating from the accumulation of potential energy that generates turbulence, secondary instabilities that support shear and zonal flows using the kinetic energy of turbulence, and tertiary instabilities that destabilize both of these flow types (Numata et al., 2007).

The structure of this work unfolds as follows: It commences with a theoretical foundation in Chapter 2, delving into the fundamental concepts of thermonuclear fusion and magnetic confinement. This chapter provides insights into the workings and physics underpinning the Tokamak mechanism designed for plasma confinement, with a dedicated section on the L-H transition. Chapter 3 explores the definition of plasma and its interaction with an electromagnetic field, elaborates on concepts such as turbulence and zonal flow, and presents the theoretical underpinnings of the Hasegawa-Wakatani model utilized. In Chapter 4, we present the tools for analyzing plasma behavior as well as their implementation. Subsequently, Chapter 5 contains the results and ensuing analyses. Finally, the report concludes in Chapter 6.

1.1 Objectives

1.1.1 General Objective

This work aims to characterize the degree of ordering of turbulent fusion plasma during its transition from low-to-high confinement through two-dimensional numerical simulations of the modified Hasegawa - Wakatani equations. We will apply information theory, more specifically entropy and complexity, to quantify the degree of disorder in the spatial patterns in the numerical simulations.

1.1.2 Specific Objectives

- To obtain the patterns of electrostatic potentials φ from the modified Hasega-Wakatani equations for different α values.
- To calculate the 2D Fourier transform from the images obtained from the electrostatic potential to generate the power spectrum of the transition for the x and y components of the velocities.
- To obtain the values of total and zonal kinetic energy to distinguish the different regimes of confinement.
- To calculate the normalized entropy of Shannon $H(t)$ and the complexity of Jesen-Shannon C_{JS}.
- To construct bifurcation diagrams of the respective properties for the control parameter α

and to analyze their behavior.

- To build the local entropy and the local complexity maps and the C-H plane.
- To analyze the obtained results and describe the transition regime.

2 Thermonuclear Fusion

2.1 Fusion Reaction

Nuclear fusion occurs naturally in stars and is responsible for energy production in the sun (Graham, 2002). The process of nuclear fusion occurs when two light nuclei combine to form a heavier nucleus, however the final mass of the resulting nucleus is slightly less than the sum of the initial masses of the reacting nuclei, this is due to the conversion of mass into energy released, this relation is explained by Einstein's famous equation (Bittencourt, 2013)

$$E = mc^2, \tag{2.1}$$

where c represents the speed of light. For this reaction to take place, the ions or heavier reactant nuclei need to have enough thermal energy to overcome the electrostatic repulsion arising from the repulsive Coulomb forces and come close sufficiently to each other for the strong nuclear force (responsible for binding the nucleons together inside the nucleus) attract them and then fuse by means of quantum tunneling, or the tunnel effect (Kikuchi et al., 2012).

One of the most important fusion reactions occurs between the isotopes of hydrogen, deuterium (D) and tritium (T), which fuse to form a Helium atom (^4He), called the α particle, releasing a neutron (n) and energy (Wesson and Campbell, 2004). Is described below

$$D + T \longrightarrow {}^4He + n + 17.6MeV. \tag{2.2}$$

Conforming to Kikuchi et al. (2012), the energy released by a nuclear fusion reaction is considerably greater than the energy from chemical reactions, since the binding energy, which holds the particles together inside the atomic nucleus, is greater than the electron binding energy, which holds atoms and molecules together.

In order to use this resource as an energy source and recreate it in a terrestrial environment, it is necessary to generate a plasma from the reactant elements of the fusion at high temperatures and confine it for long enough for the reactions to take place (Kikuchi et al., 2012). For Dolan (2013b), this confinement can be accomplished in six different ways:

- Solid walls: Used for low-temperature plasma, these are contained by means of the recipients to which they are confined, such as glass or metal tubes. For hot plasma, prolonged contact with the walls cools them down and damages the boundary walls.

- Gravity: A method of confinement that occurs in stars, in which they use their own gravitational field to contain the plasma generated.
- Inertia: Fusion is obtained by means of micro-explosions of the reactant fuel induced by laser or particle beams, these compress the fuel increasing the pressure and temperature, the inertia then restricts the rate of expansion of the plasma confining it.
- Eletromagnetic waves: Used for low-pressure plasma, it uses radiofrequency and microwaves for containment. Electromagnetic waves can also be used to increase magnetic confinement.
- Electrostatic fields: The plasma is confined by an electrostatic potential well generated by an electric field, where the positive potentials repel the ions that are accelerated towards the center of the fusion reactor, while the electrons are repelled by the negative potential of the electrodes; usually polarized concentric spherical grids with high voltages are used for this confinement.
- Magnetic fields: The confinement takes place by means of the magetic field, since the Lorentz force (the result of the superposition of electromagnetic forces on a moving charged particle) spreads the movement of electrons and ions around the field lines, preventing the particles from penetrating it. This mechanism will be discussed in more detail in section 2.2.

2.2 Magnetic Confinement

Magnetic confinement occurs through the interaction of the magnetic field with the charged particles in the plasma. This mechanism restricts the movement of the particles across the field lines, but allows them to move freely along them. This is due to the Lorentz force, $\vec{F} = q\vec{v} \times \vec{B}$, which forces ions and electrons to spiral around these field lines (Conn, 2008).

According to Najmabadi and Prager (2007), part of the fusion problem lies in obtaining a magnetic field configuration that effectively confines the plasma inside. To this end, the authors defined three criteria that this configuration must meet in order to be considered successful:

1. The plasma must be in a state of equilibrium invariant in time;
2. This equilibrium must be macroscopically stable;
3. Energy losses from the plasma to the wall must be small.

For the plasma to be in equilibrium, magnetic forces must counteract the expansive pressure force caused by the thermal energy of all present particles. Furthermore, this state of equilibrium must be stable, meaning the plasma must return to its initial state even after experiencing small disruptions. Conversely, an unstable plasma would not return to its initial state and would escape the magnetic field after such disruptions.

Finally, the stable equilibrium must be maintained indefinitely as long as the plasma's energy losses are balanced with the energy input into the system. If the losses are significant, achieving ignition (the moment the fusion reaction becomes self-sustained) may not be possible, resulting in energy diffusion along the magnetic field line, where energy is carried from the hot core to the walls (Najmabadi and Prager, 2007).

In this manner, we can classify magnetic field configurations into two types based on their geometry and topology: open linear configurations and closed toroidal configurations (Dolan, 2013b). In the case of open-type configurations, confinement occurs through the use of mirrors and magnetic cusps, as shown in Figure 2.1.

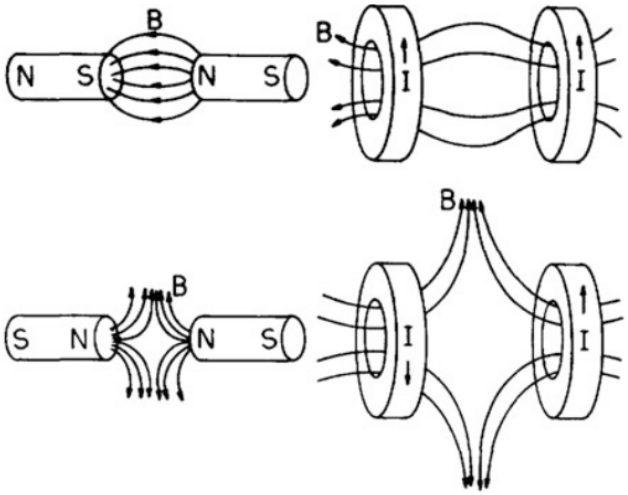

Figure 2.1. Representation of magnetic mirrors (top) and spindle cusps (bottom), both fields generated on the left by magnets and on the right by circular magnetic coils. Source: (Dolan, 2013b)

The plasma ions are confined in the center of the magnetic mirrors. As they move towards the coils, they experience an increase in field strength. In this region, the particle's rotational velocity component ($v_{\perp 0}$) increases while its parallel component ($v_{\parallel 0}$) decreases until it reaches zero. Then, the particle is reflected back to the center, similar to a mirror effect (Dolan, 2013b). The ions and electrons restricted in this arrangement would oscillate between areas of high magnetic fields as depicted in Figure 2.2, delineated by the letters 'a' and 'b'.

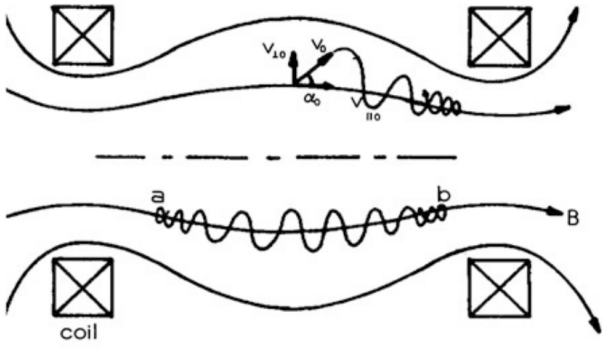

Figure 2.2. Trajectory of particles inside magnetic mirrors. Source: (Dolan, 2013b)

Although some particles are reflected by the high magnetic fields, others manage to escape due to their high velocities along the field lines. Consequently, confinement is limited to the time required for Coulomb collisions to increase the particles' $v_{\|0}$, making it impractical to achieve substantial energy gains (Dolan, 2013b). To avoid these losses, we can adopt a closed magnetic field configuration, altering the linear topology to a toroid.

According to Chen (2012, 2016), in a simple toroidal magnetic field, electrons and ions drift outwards, this charge separation indicates poor confinement. However, if the magnetic field lines are distorted, these drifts become neutralized. There are two mechanisms that can provide this twisting effect: In tokamaks, a plasma current is induced in a toroidal direction and a poloidal magnetic field is generated, the combination of the poloidal and toroidal fields gives rise to helical magnetic field lines, as discussed in Section 2.3; the second mechanism is Stellarators, which deploy helical coils to twist the magnetic field, reducing the need for a strong toroidal plasma current and allowing long term operation (Dolan, 2013b).

2.3 Tokamaks

Magnetic confinement fusion stands out as the preeminent approach to effectively trapping plasma particles along magnetic field lines - this concept is applied in practice in reactors of the tokamak type (Kikuchi et al., 2012). The term tokamak is an acronym of the Russian words "Тороидальная камера с магнитными катушками", which in free translates means "toroidal chamber with magnetic coils". Created in the then Union of Soviet Socialist Republics, the now extinct USSR, in 1955, the first model was called the TMB and little is known about it due to the secretive nature of the project at the time (Kadomtsev, 1988).

Within a tokamak, plasma takes on a toroidal shape. This geometry is established by encircling a solenoidal array of ring-like coils, effectively creating a toroidal magnetic field. However, a purely toroidal magnetic field proves inadequate for containing plasma particles due to the curvature of the field lines, which induces opposing drifts in ions and electrons, resulting in charge separation. This charge separation, in turn, generates an electric field that accelerates the rapid loss of plasma towards the chamber walls (Chen, 2012, 2016; Kikuchi et al., 2012).

To prevent the occurrence of charge separation, an additional magnetic field component is required, one that encircles the minor cross-section of the torus, known as the poloidal magnetic field (Kikuchi et al., 2012). In tokamaks, the creation of the poloidal magnetic field involves inducing a toroidal current within the plasma itself. This leads to the formation of spiraling magnetic field lines resulting from both the toroidal and poloidal components, extending infinitely around the torus and giving rise to nested toroidal surfaces. These surfaces collectively constitute globally closed magnetic flux surfaces.

However, this toroidal plasma configuration, influenced by both toroidal and poloidal magnetic fields, encounters a hoop force, which exerts pressure to expand the plasma torus radially outward. Achieving radial equilibrium necessitates the introduction of vertical magnetic fields through vertical field coils, which are typically current-carrying rings aligned concentrically with the torus (Kikuchi et al., 2012).

In summary, confinement in tokamaks occurs as shown in Fig. (2.3). Toroidal field coils with a specific shape are employed to establish a magnetic field oriented in the toroidal direction. These coils delineate the toroidal shape within which the plasma will be confined. To induce a changing flux through the center of the torus, a current is passed through the inner poloidal field coils. Essentially, the inner poloidal field coils function as the primary winding in a transformer, while the plasma itself serves as the secondary winding. This setup induces a toroidal current within the plasma, which, in turn, generates a poloidal magnetic field. This poloidal magnetic field combines with the toroidal field to produce the resultant helical magnetic field

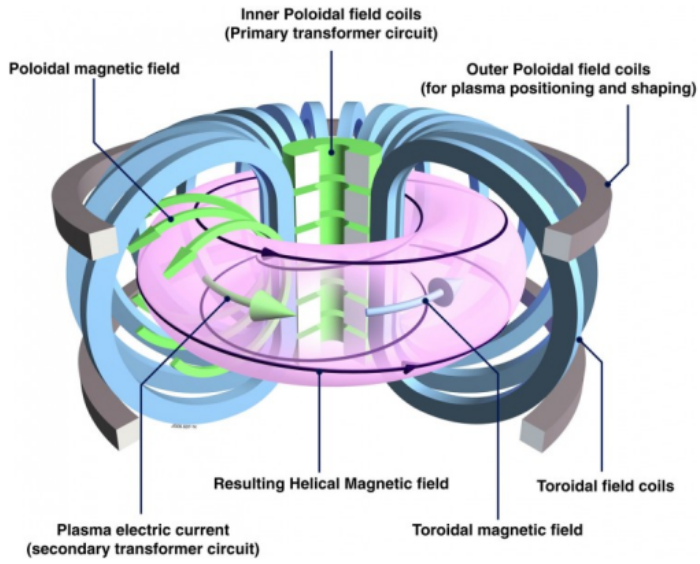

Figure 2.3. Schematic representation of a tokamak. Source: (Kikuchi et al., 2012)

The plasma finds its confinement within a designated region known as the plasma column, encircled by what's termed the last closed (magnetic) flux surfac (LCFS) and is frequently utilized to delineate the plasma boundary (Dewhurst, 2010). In the cross-section of the toroidal chamber, the radial position of this surface is determined by either the limiter—a material at the plasma edge intercepting field lines extending beyond its position—or a diverter, a magnetic field configuration that confines the plasma within an area marked by a separatrix. The region between the LCFS and the chamber wall is commonly referred to as the Scrape-Off Laye (SOL). This nomenclature arises from the magnetic field lines that are exposed and scrape against the limiter (or diverter) or the chamber wall within this zone (Stangeby et al., 2000). These two configurations are illustrated below

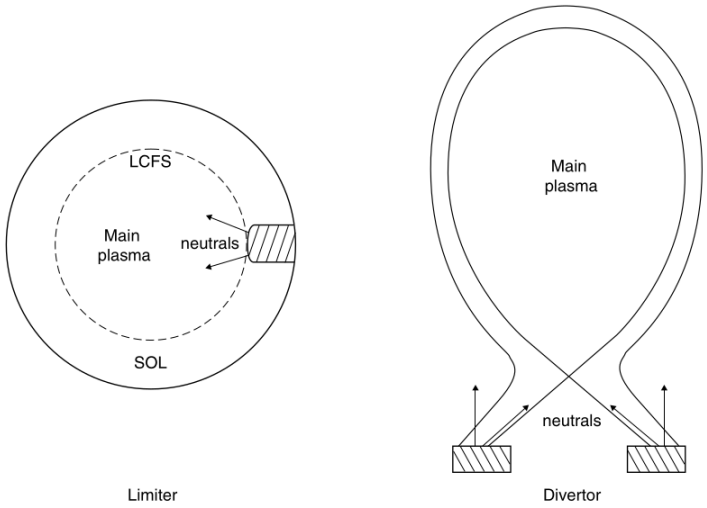

Figure 2.4. Configuration of tokamaks utilizing limiter (Left) and diverter (Right).
Source: (Stangeby et al., 2000)

The edge region of plasma assumes a crucial role in controlling the overall plasma confinement. In many tokamak plasma scenarios, two main confinement states emerge: L-mode, representing low confinement, and H-mode, indicating high confinement. Under certain operational conditions, there is a sudden improvement in confinement, transitioning from L-mode to H-mode. Consequently, significant temperature and density gradients accumulate in proximity to the plasma edge, similar to the creation of a transport barrier (Wesson and Campbell, 2004; Dewhurst, 2010).

2.4 L-H Transition

In tokamaks, as well as in other magnetic confinement devices, plasma can spontaneously transition from a low-confinement (L) to a high-confinement (H) state due to the suppression of turbulence and the formation of a transport barrier in the plasma edge region, this is called the L-H transition (Numata et al., 2007; Burrell, 1997; Guosheng and Xingquan, 2017).

This transition was first reported by Wagner et al. (1982) in the ASDEX tokamak where the H mode was observed (Wagner et al., 1982). This confinement regime is marked by longer confinement time, reduced plasma fluctuations, and the creation of transport barriers in the region. When the input power exceeds the called limit P_{th} of the confinement device - which is directly proportional to the toroidal magnetic field B_t and the plasma density n, meaning that $P_{th} \propto B_t n$ - the L-H transition occurs (Diamond et al., 1994).

According to Numata et al. (2007), this suppression of turbulent transport is due to a nonlinearly self-generated poloidal $E \times B$ shear flow, also called zonal flows. This in turn, according to the author, plays a crucial role in turbulent transport, reducing anomalous transport, absorbing the energy of drift waves and delimiting the turbulent region characterized by eddies (Numata et al., 2007).

3 Plasma

3.1 Fundamentals

The word plasma is of Greek origin and means "something molded or manufactured" (Bittencourt, 2013). The term was coined by Langmuir (1928) in his article "Oscillations in ionized gases" published in Proceedings of the National Academy of Sciences in 1928, to describe the region containing balanced charges of ions and electrons. Also known as the fourth state of matter, is found in nature through atmospheric electrical discharges, in polar auroras, stars, nebulae and more. (Chen, 2016).

Plasma can be defined as an ionized gas made up of ions and electrons (Wesson and Campbell, 2004). To determine this degree of ionization is used the Saha equation described below

$$\frac{n_i}{n_n} \approx 2.4 \times 10^{21} \frac{T^{3/2}}{n_i} \exp\left(-\frac{U_i}{k_B T}\right), \tag{3.1}$$

where n_i represents the density of ions, n_n the density of neutral atoms, T the temperature of the gas, U_i the ionization energy and k_B the Boltzmann constant.

When analyzing the equation (3.1), it can be seen that as the temperature rises, the n_i/n_n component remains low until the ionization energy is slightly lower than the $k_B T$ term, so the degree of ionization rises abruptly and the gas can then be considered to be in a plasma state.

However, not every ionized gas can be considered a plasma. With this, according to Chen (2016) plasma can be defined as "a quasi-neutral gas of charged and neutral particles that exhibit collective behavior". In this way, the two fundamental characteristics described are evident: quasi-neutrality and collective behavior.

For the first, macroscopic neutrality is implied, in which the densities of ions and electrons are sufficiently close to the point of considering $n_i \simeq n_e \simeq n$, with n being the common density, generalized as the plasma density, however this does not make it completely neutral, to the point where the electromagnetic forces disappear (Chen, 2016).

With regard to collective behavior, there is the movement of charged particles within the plasma, which leads to the generation of local concentrations of positive or negative charges giving rise to electric fields, this movement also results in electric current, which in turn induces magnetic fields and thus influences the movement of more distant particles denoting the so-called "collective behavior".

From these two characteristics it is possible to extract three conditions that must be met in

order to consider an ionized gas as a plasma. These are:

3.1.1 Debye Shielding

To maintain its quasi-neutrality, plasma has the ability to shield electrical potentials applied to it. This is due to the free charges present; when an external potential is applied or appears spontaneously through the movement of particles, an accumulation of charges arises around it, creating a shield and ensuring quasi-neutrality (Chen, 2016).

Debye's shielding is represented in the following figure, in which there are two charged spheres, one with a positive charge and the other with a negative electrical charge, both immersed in a plasma, and the formation of an accumulation of opposite charges around the spheres is observed, characterizing this shielding.

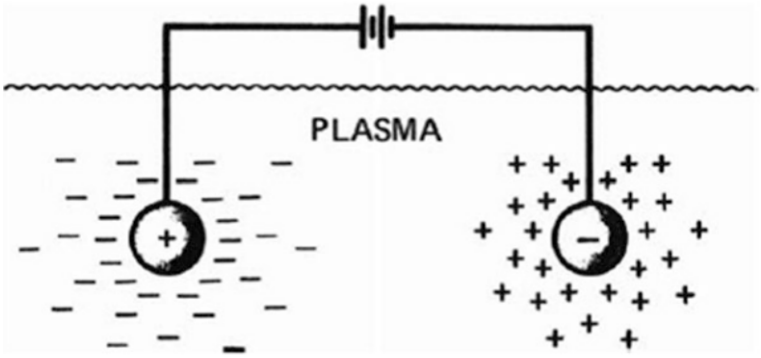

Figure 3.1. Debye shield. Source: (Hasegawa and Wakatani, 1983)

The efficiency of this shielding is restricted to a radius of action in which the thermal energy of the particle equals the electrostatic potential of the barrier; this radius, or thickness of the shielding, is called the Debye length and can be represented as

$$\lambda_D \equiv \left(\frac{\varepsilon_0 k_B T}{n e^2} \right)^{1/2}, \tag{3.2}$$

where ε_0 is the vacuum permittivity constant, k_B is the Boltzmann constant, T is the particle temperature, n is the plasma density and e is the Euler number. With this, the first criterion for characterizing a plasma can be defined

$$\lambda_D \ll L, \tag{3.3}$$

in which L is the dimension of the system. It can then be concluded that the Debye shield must have a thickness less than the size of the system to ensure the quasi-neutrality of the whole.

3.1.2 Debye Sphere

For the Debye shield to be effective, there must be enough particles around the potential (Bittencourt, 2013). Thus, considering the Debye length as the radius of a sphere of the same name, we can consider the number of particles inside it to be equal to

$$N_D = n\frac{4}{3}\pi\lambda_D^3. \tag{3.4}$$

With this, the second criterion for the definition is described as

$$N_D \ggg 1. \tag{3.5}$$

3.1.3 Collision Frequencies

In order to ensure the characteristic of collective behavior, it is necessary for the oscillation frequency of the plasma to be higher than the frequency of collisions with the neutral atoms, otherwise the collisions would force the electrons to enter into equilibrium with the neutral particles and, thus, it would be a neutral gas, since the collisions between the electrons and the neutral particles tend to dampen the collective oscillations (Bittencourt, 2013).

Thus, considering ω as the typical frequency of plasma oscillations and τ as the average time between collisions with neutral atoms, the third condition is described as

$$\omega\tau > 1. \tag{3.6}$$

3.2 Particle Motion in the Presence of an Uniform Electromagnetic Field

To analyze the motion of a charged particle considering the action of both electric and magnetic fields, which are invariant in time and uniformly distributed in space. We can use the nonrelativistic equation of motion described below:

$$m\frac{d\vec{v}}{dt} = q(\vec{E} + \vec{v} \times \vec{B}) \tag{3.7}$$

where m is the mass and q is the charge of the particle, which move with velocity $\vec{v}$, under the electric and magnetic fields, $\vec{E}$ and B, respectively. Considering the components parallel and perpendicular to the magnetic fields of $\vec{v}$ and $\vec{E}$, the Eq. (3.7) can be rewrite into two component equations:

$$m\frac{d\vec{v}_\parallel}{dt} = q\vec{E}_\parallel \tag{3.8}$$

$$m\frac{d\vec{v}_\perp}{dt} = q(\vec{E}_\perp + \vec{v}_\perp \times \vec{B}) \tag{3.9}$$

For Eq. (3.8), it can be solve it by separating the variables $d\vec{v}_\parallel/dt$ and integrating to both sides of the equality, thus achieving the equation describing its velocity $\vec{v}_\parallel$, integrating the

obtained equation 3.10, we obtain its position $r_{\parallel}$ expressed by 3.11.

$$\vec{v}_{\parallel}(t) = \left(\frac{q\vec{E}_{\parallel}}{m}\right) t + \vec{v}_{\parallel}(0) \tag{3.10}$$

$$r_{\parallel}(t) = \frac{1}{2}\left(\frac{q\vec{E}_{\parallel}}{m}\right) t^2 + \vec{v}_{\parallel}(0)t + r_{\parallel}(0). \tag{3.11}$$

Concerning the second equation of motion, as given by (3.9), it is appropriate to separate the velocity $\vec{v}_{\perp}$ into two constituent components: $\vec{v}'_{\perp}$ and $\vec{v}_E$. Notably, $\vec{v}_E$, also known as electromagnetic drift velocity, constitutes a constant velocity within the plane perpendicular to the magnetic field $\vec{B}$ and $\vec{v}'_{\perp}$ represents the particle's velocity as observed from a reference frame moving at the velocity $\vec{v}_E$. Hence,

$$\vec{v}_{\perp}(t) = \vec{v}'_{\perp}(t) + \vec{v}_E. \tag{3.12}$$

Substituting (3.12) into (3.9) and considering $\vec{E}_{\perp} = -\left(\frac{\vec{E}_{\perp}\times\vec{B}}{B^2}\right) \times \vec{B}$, we get

$$m\frac{d\vec{v}'_{\perp}}{dt} = q\left(\vec{v}'_{\perp} + \vec{v}_E - \frac{\vec{E}_{\perp}\times\vec{B}}{B^2}\right) \times \vec{B}. \tag{3.13}$$

It is known that the drift velocity $\vec{v}_E = \vec{E}_{\perp} \times \vec{B}/B^2$, so the equation (3.13) becomes

$$m\frac{d\vec{v}'_{\perp}}{dt} = q(\vec{v}'_{\perp} \times \vec{B}). \tag{3.14}$$

With this, we can conclude that the particle's movement in the plane perpendicular to B is solely affected by the magnetic field. The circular motion of the particle, for $\vec{v}'_{\perp}$, is described by the cyclotron frequency ω_c, and its radius r_c, also called the Larmor radius. Thus, the equation results

$$\vec{v}'_{\perp} = \omega_c \times r_c, \tag{3.15}$$

where the cyclotron frequency described by $\omega_c = |q|\vec{B}/m$, represent the angular frequency of circular motion. Therefore, the radius of this motion is defined by the particle orbit being $r_c = \vec{v}_{\perp}/\omega_c$, i.e $r_c = m\vec{v}_{\perp}/|q|\vec{B}$.

Based on the findings up to this point, it is evident that the resultant particle trajectory can be characterized as a combination of two fundamental motions: circular motion within the plane perpendicular to $\vec{B}$; and uniform motion with a constant velocity $\vec{v}_E$ that is perpendicular to both $\vec{B}$ and $\vec{E}_{\perp}$.

Additionally, there is an element of uniform acceleration along $\vec{B}$, quantified as $q\vec{E}/m$. The particle's velocity can be mathematically expressed in vector form, free from any specific

coordinate system, as follows:

$$\vec{v}(t) = \vec{v}_{\perp}(t) + \vec{v}_{\parallel}(t) \tag{3.16}$$

$$\vec{v}(t) = \vec{v}'_{\perp}(t) + \vec{v}_E + \vec{v}_{\parallel}(t) \tag{3.17}$$

$$\vec{v}(t) = \omega_c \times r_c + \frac{\vec{E}_{\perp} \times \vec{B}}{B^2} + \frac{q\vec{E}_{\parallel}}{m}t + \vec{v}_{\parallel}(0) \tag{3.18}$$

The particle's motion within the plane perpendicular to $\vec{B}$ typically takes the form of a cycloid, as exemplified in Fig. 3.2. According to Bittencourt (2013) this cycloidal motion occur because simultaneously with the magnetic force, the electric force $q\vec{E}_{\perp}$ accelerates the particle, either boosting or reducing its velocity. This effect hinges on the particle's motion relative to the direction of $\vec{E}_{\perp}$ and the charge's sign.

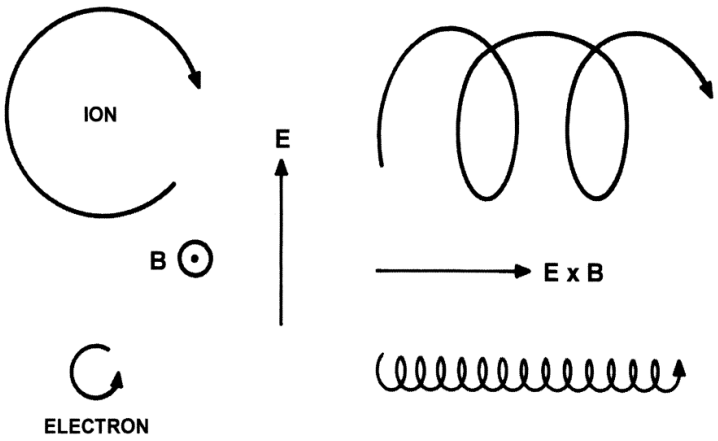

Figure 3.2. Cycloidal trajectory of particles when subjected to crossed electric and magnetic fields. Source: (Bittencourt, 2013)

3.2.1 Particle Drifts

In magnetized plasma, different drift phenomena may cause single particles' guiding centers to travel along the magnetic field lines. The general equation for particle drift is commonly expressed by adding a force, $\vec{F}$, to the equation of motion, (3.7). Through algebraic manipulation, we can obtain the equation:

$$\vec{v}_f = \frac{1}{q}\frac{\vec{F} \times \vec{B}}{B^2}, \tag{3.19}$$

where q its the charge of particle, and $\vec{B}$ the magnetic field. These drifts can occur due to the presence of an electric field perpendicular to B ($E \times B$), a gradient in the magnetic field (∇B), or the curvature of the magnetic field, as well as a transient electric field (Wesson and Campbell, 2004). Which will be discussed in detail below.

3.2.1.1 $\vec{E} \times \vec{B}$ drift

In the presence of an electric field, particle motion is associated with Larmor's circular motion and the drift of the guiding center. This confers cycloidal trajectory to the particles, as discussed in the previous section 3.2. In this way, the electromagnetic drift is induced by the electric force qE imparted by the electric field. By substituting Eq. (3.19), the drift velocity can be determined.

$$\vec{v}_d = \vec{v}_E = \frac{\vec{E} \times \vec{B}}{B^2}. \tag{3.20}$$

This particular drift remains unaffected by the mass and charge of individual particles, resulting in the collective drift of the entire plasma in the same direction (Chen, 2016). The establishment of an electric field for this drift can occur locally due to fluctuations and plays a significant role in the occurrence of drift waves, as will be discussed in the following sections.

3.2.1.2 $\nabla|B|$ drift

The presence of a magnetic field, with a transverse gradient can lead to a drift perpendicular to both. This is due to the size of the radius of curvature of the particle's orbit associated with the strength of the magnetic field, i.e. for a strong magnetic field the radius of curvature is small (Wesson and Campbell, 2004).

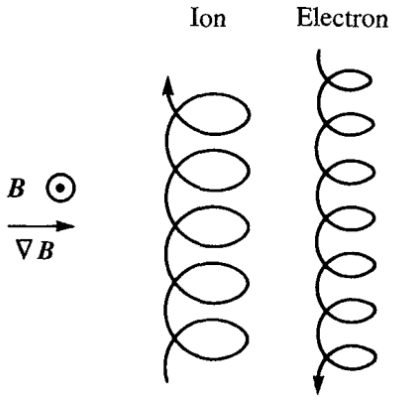

Figure 3.3. Particles drifts in opposite directions under a gradient of $|B|$ perpendicular to B. Source: (Wesson and Campbell, 2004)

Thus, the magnitude of the drift can be expressed from the equation of motion for a magnetic field oriented in the z-direction and its gradient in the y-direction,

$$m\frac{d\vec{v}_y}{dt} = q\vec{v}_x\vec{B}. \tag{3.21}$$

Assuming a small gradient of $|B|$, such that the magnetic field variation across the Larmor radius is significantly smaller than B itself, the magnetic field can be expressed as $\vec{B} = \vec{B}_0 + \frac{d\vec{B}}{dy}y$ where $y = 0$ is at midplane of the orbit.

When considering the entire velocity component perpendicular to the direction of the mag-

netic field, it can be observed as the outcome of sum the velocity related to $\nabla|B|$ and the perpendicular velocity. The resulting expression is

$$\vec{v}_x = \vec{v}_{x0} + \vec{v}_d, \tag{3.22}$$

rewriting Eq. (3.21) inserting the expressions for $\vec{v}_x$ and $\vec{B}$, we get

$$m\frac{d\vec{v_y}}{dt} = -q\vec{v}_{x0}\left(\vec{B}_0 + \frac{d\vec{B}}{dy}y\right) - q\vec{v}_d\vec{B}_0 - q\vec{v}_d\frac{d\vec{B}}{dy}y, \tag{3.23}$$

as $\vec{v}_d$ and $d\vec{B}/dy$ are very small, we can ignore the last term of the equation (Gallagher, 2013). In this way, for $\vec{v}_{x0} = \vec{v}_\perp \sin(\omega_c t)$ and $y = \frac{\vec{v}_\perp}{\omega_c}\sin(\omega_c t)$, the Eq. (3.23) becomes

$$\frac{m}{q}\frac{d\vec{v}_y}{dt} = -\vec{v}_\perp \sin(\omega_c t)\left(\vec{B}_0 + \frac{d\vec{B}}{dy}\frac{\vec{v}_\perp}{\omega_c}\sin(\omega_c t)\right) - \vec{v}_d\vec{B}_0. \tag{3.24}$$

for time average of this equation, considering $\langle d\vec{v}_y/dt\rangle = 0$, the drift velocity in the x-direction is equal to

$$\vec{v}_d = -\frac{1}{2}\frac{\vec{v}_\perp}{\omega_c\vec{B}}\frac{d\vec{B}}{dy}\vec{v}_\perp,$$

in vector form

$$\vec{v}_d = \frac{1}{2}\frac{v_\perp}{\omega_c}\frac{\vec{B}\times\nabla|B|}{B^2}v_\perp, \tag{3.25}$$

the sign of the equation depends on the particle being analyzed. As a result, the $\nabla|B|$ drift generates a drift in opposite directions for particles with different electric charges, as shown in Fig. 3.3 (Wesson and Campbell, 2004).

3.2.1.3 Curvature drift

Curvature drift occurs when the guiding center of a particle follows the curvature of the magnetic field lines so that it undergoes a drift perpendicular to the plane of curvature, as shown in Fig. 3.4.

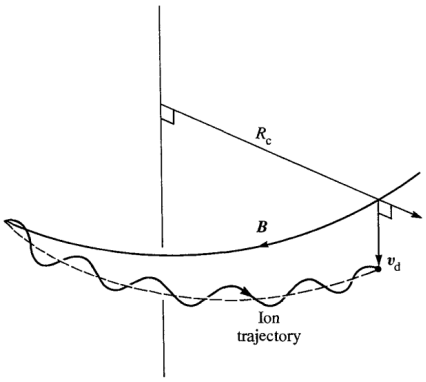

Figure 3.4. Ion drift due to the curvature of the magnetic field. Source: (Wesson and Campbell, 2004)

As of motion equation, 3.7, considering the motion of the particle with angular velocity $\vec{v}_{\parallel}/R$, being $\vec{v}_{\parallel}$ the velocity parallel to the field and R the radius of curvature of the field lines. For the centrifugal force $m\vec{v}_{\parallel}^2/R$ acting on the particle, the equation results in

$$m\frac{d\vec{v}}{dt} = \frac{m\vec{v}_{\parallel}^2}{R}i_c + q(\vec{v}\times\vec{B}), \tag{3.26}$$

where i_c is unit vector along the radius. Thus, according to Eq. (3.19), para $\vec{F} = m\vec{v}_{\parallel}^2/R$, the curvature drift is given by

$$\vec{v}_d = \frac{\vec{v}_{\parallel}^2}{\omega_c R}. \tag{3.27}$$

The cyclotron frequency ω_c will determine the sign of the particle in the above equation, since ions and electrons drift in opposite directions, so for ions $i_c\times\vec{B}$. In the absence of electric current, both the $\nabla|B|$ drift and the curvature drift behave in the same way, so for $\nabla|B| = -i_c\vec{B}/r$ the drift is given by

$$\vec{v}_d = \frac{1}{2}\frac{\vec{v}_{\perp}}{\omega_c R}$$

associating both derivatives found, we obtain

$$\vec{v}_d = \frac{\vec{v}_{\parallel}^2 + \frac{1}{2}\vec{v}_{\perp}^2}{\omega_c R} \tag{3.28}$$

with vector form

$$\vec{v}_d = \frac{\vec{v}_{\parallel}^2 + \frac{1}{2}\vec{v}_{\perp}^2}{\omega_c}\frac{\vec{B}\times\nabla|B|}{B^2} \tag{3.29}$$

Both the gradient drift of the magnetic field modulus ($\nabla|B|$) and the curvature drift are responsible for the drift of particles inside toroidal magnetic fields, as illustrated in Fig (3.5). The tendency for particles to drift in a toroidal magnetic field ($\vec{B}_t$) is compensated for by the insertion of the poloidal magnetic field, see Section 2.3. The electrons flowing along the field lines neutralize the electric field generated by the separation of charges, consequently reducing the effects of the electromagnetic drift $\vec{v}_E$ (Dolan, 2013a).

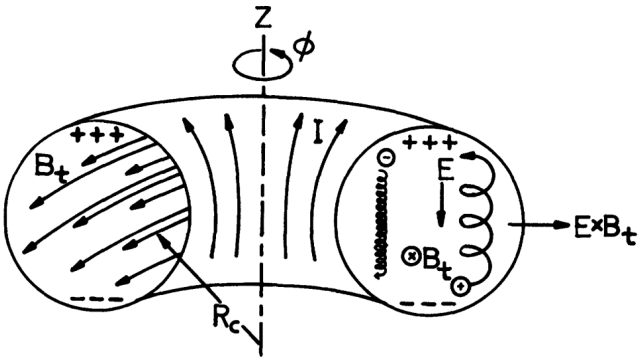

Figure 3.5. Particle drifts in a toroidal magnetic field. Source: (Jassby, 1977)

3.2.1.4 Polarization drift

Polarization drift occurs when an electric field perpendicular to the magnetic field changes with time. A polarization current proportional to $d\vec{E}/dt$ results from the drift of ions and electrons in opposite directions Wesson and Campbell (2004). This drift is illustrated below:

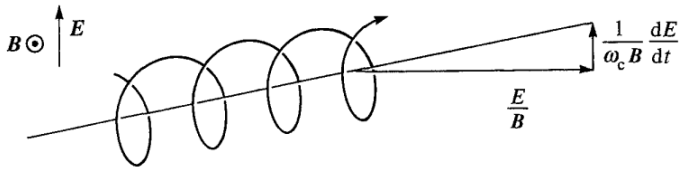

Figure 3.6. Polarization drift of an ion. Source: (Wesson and Campbell, 2004)

Considering that the acceleration of the electric field is the result of the derivative of the electric drift velocity v_E, which is given by

$$\frac{d}{dt}\vec{v}_E = \frac{d}{dt}\frac{\vec{E}\times\vec{B}}{B^2}. \tag{3.30}$$

From the acceleration found, we can deduce that the force responsible for the drift is given by

$$\vec{F} = m\frac{d}{dt}\frac{\vec{E}\times\vec{B}}{B^2}, \tag{3.31}$$

substituting into the equation (3.19), the polarisation drift is

$$\vec{v}_d = \frac{1}{\omega_c B_0}\frac{d\vec{E}}{dt}. \tag{3.32}$$

The drift occur in the same direction of the current $d\vec{E}/dt$ for ions and in other for electrons. The polarization drift causes charge separation, as $\nabla|B|$ drift creates a time-varying electric field, which in turn induces a polarization drift (Gallagher, 2013).

3.3 Turbulence

Turbulence represents a state of fluid motion distinguished by its unpredictability across a broad spectrum of temporal and spatial scales. This state of motion, seemingly chaotic, is characterized by a succession of cascading eddies. Initially, the system's energy is driven on larger scales, forming substantial eddies that subsequently fragment into numerous smaller ones. This fragmentation process continues until the eddies reach a scale where energy dissipation can occur due to viscosity (Dewhurst, 2010; Gallagher, 2013).

In fluid dynamics, a control parameter known as the Reynolds number can be obtained by

balancing the nonlinear and dissipative terms within the momentum equation. Given by

$$Re = \frac{vL}{\nu}, \tag{3.33}$$

where v is the fluid velocity, L is a length scale, and ν is viscosity. In general, high Reynolds numbers are associated with turbulent behavior, while low Reynolds numbers result in laminar flow. This distinction arises from the ability of the Reynolds number to measure the relative dominance of the nonlinear term ($\vec{v}\nabla\vec{v}$) of Navier-Stokes equations, (3.34), compared to the linear term ($\nu\nabla^2\vec{v}$) within the system. At low Reynolds numbers, the Navier-Stokes equation behaves effectively linearly, while at high Reynolds numbers the nonlinear terms become the primary driving force behind the evolution of the system.

$$\partial_t\vec{v} + \vec{v}\nabla\vec{v} = -\nabla p + \nu\nabla^2\vec{v}, \tag{3.34}$$

$$\nabla\vec{v} = 0. \tag{3.35}$$

Similar parameters are frequently employed in the context of magnetized plasma, where the Reynolds number (Re) and its magnetic analog, denoted as Rm, are defined (Biskamp, 1997). Nevertheless, these constructs are not equivalent, owing to the presence of non-diffusive dissipation processes, such as Landau damping, which operate on scales significantly smaller than the conventional collisional dissipation (Dewhurst, 2010).

According to Dewhurst (2010), in the Richardson-Kolmogorov perspective on three-dimensional hydrodynamic turbulence depicts a fluid undergoing a process of fragmentation into large eddies as a result of instability in the mean flow. These large eddies, in turn, experience their own instability and disintegrate into smaller eddies, continuing this cascade of energy transfer from larger to smaller scales.

Finally, at a very small scale, as the Reynolds number (Re) approaches about 1, the influence of viscosity becomes significant and leads to the dissipation of energy. The scales at which this cascade transpires, denoted as 'k', are commonly referred to as the 'inertial range. Therefore, energy spectrum of the system for three-dimensional isotropic, homogeneous and incompressible turbulence, taken out of Frisch and Kolmogorov (1995) is

$$E(k) \sim k^{-\frac{5}{3}}. \tag{3.36}$$

The 3D turbulence model used by Frisch and Kolmogorov (1995) is not suitable for tokamak physics. One of the reasons for this mismatch is the presence of a magnetic field, which gives the turbulence a distinct direction. The high-speed motion of electrons along magnetic field lines tends to dampen parallel gradients, effectively rendering turbulence in tokamaks 2D (Gallagher, 2013). In this scenario, the enstrophy, which is the square of the vorticity, is also conserved. In the context of the plasma physics considered here, enstrophy takes the following form

$$\varepsilon = |\nabla^2\varphi|^2, \tag{3.37}$$

being φ is the electrostatic potential. When considering the conservation of enstrophy, the system exhibits two distinct cascades, as discussed by Kraichnan (1967). In this context, energy embarks on an 'inverse cascade,' directing its transfer towards large, low-wavenumber structures, including vortices and potentially zonal flows (Gallagher, 2013).

3.3.1 Resistive Drift Waves

Turbulence in the context of fusion plasma is commonly addressed through a formulation centered on drift waves and drift instabilities (Gallagher, 2013). Drift waves are of particular importance due to their prevalence in the edge regions of thermonuclear fusion plasma. These micro-scale drift wave instabilities are believed to be the primary drivers of most of the anomalous transport observed in tokamaks (Dewhurst, 2010; Pushkarev, 2013a).

Drift waves are characterized by their low frequency, when compared to the cyclotron frequency of the ion, and are instigated by gradients in either density or temperature. In general, they exhibit an electrostatic nature, described as $E = -\nabla\varphi$, and encompass the principles of two-fluid physics (Dewhurst, 2010). From the Branginskii momentum equation for electrons, given by

$$mn\left(\frac{\partial}{\partial t} + \vec{u}\cdot\nabla\right)\vec{u} = nq(\vec{E} + \vec{u}\times\vec{B}) - \nabla p - \nabla\cdot\vec{\Pi} + \vec{R} \tag{3.38}$$

where $p = nT$ is the scalar pressure, $\vec{\Pi}$ is the component of the pressure tensor, $\vec{R}$ is the transfer of momentum, q is the heat flux, and $\vec{u}$ is the velocity of particle. Considering an isothermal and quasi-neutral plasma, where $n_e = n_i = n$. The motion equation, obeying the Boltzmann relation, we get

$$\frac{\tilde{n}}{n_0} = \frac{e\varphi}{T_e} \tag{3.39}$$

being n_0 the constant background density, $\tilde{n}$ is the perturbation of density and φ the electrostatic potential of this perturbation. Thereat, the mechanism of the resistive drift waves can be seen in the Fig. 3.7

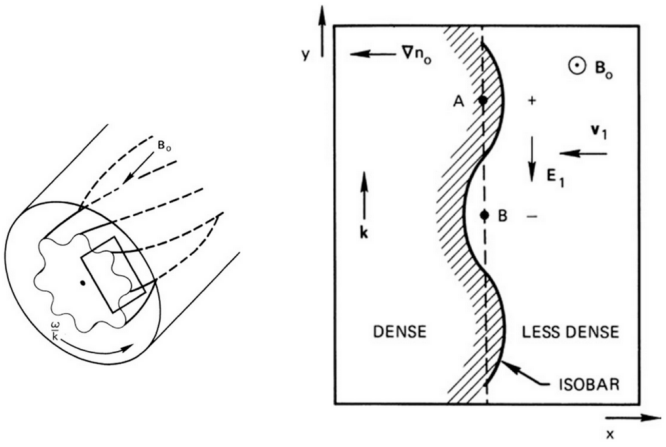

Figure 3.7. Geometry of a drift instability, on the left, and Drift-wave mechanism in details, on the right. Source: (Chen, 2016)

In Figure 3.7 we observe a plasma in a plane perpendicular to a magnetic field, denoted B_0, with a pronounced density gradient ∇n_0 in the negative x-direction. The figure illustrates a small density perturbation, represented by a continuous line, which corresponds to a perturbation in the potential φ. This perturbation leads to the generation of an electric field, denoted E_1, directed from positive to negative potential, accompanied by a corresponding $\vec{E}\times\vec{B}$ drift velocity, v_1. The direction of this $\vec{E}\times\vec{B}$ velocity varies along the perturbation, resulting in a displacement of the entire density perturbation in the positive y-direction. Consequently, a drift wave can propagate along the wave vector k, which is perpendicular to both the magnetic field and the density gradient.

When the electron parallel response follows an adiabatic behavior, as described by Equation (3.39), the density and potential fluctuations associated with drift waves remain in phase, resulting in no overall density transport. However, when the electron response deviates from adiabatic conditions, perhaps due to factors such as resistivity, the potential and density fluctuations can fall out of phase, rendering drift waves unstable. This phenomenon is identified as the drift wave instability, which, through nonlinear interactions, ultimately gives rise to drift wave turbulence (Dewhurst, 2010).

3.3.2 Zonal Flow

Zonal flows, characterized by mean azimuthally symmetric band-like shear flows, are a commonly observed phenomenon both in the nature and within laboratory (Diamond et al., 2005). Notable examples include the atmospheric belts and zones on Jupiter, as well as the terrestrial atmospheric jet streams. In laboratory contexts, such as tokamak plasma, zonal flows are a prominent feature within magnetic confinement devices, exerting significant influence over the formation of transport barriers and their dynamic behavior. This influence is evident in the transition from sheared $\vec{E}\times\vec{B}$ flows to the development of L-mode confinement and also plays a pivotal role in the L-to-H transition (Horton, 1999; Diamond et al., 2005).

According to Diamond et al. (2005) the zonal flow characterizes a toroidally symmetric electric field perturbation within a toroidal plasma. It remains constant on magnetic surfaces while exhibiting rapid variations in the radial direction, as depicted in Figure 3.8. The accompanying $\vec{E}\times\vec{B}$ flow operates in the poloidal direction, with its polarity changing as a function of radius. Essentially, the zonal flow represents a significantly asymmetric limit of a convective cell. The crux of zonal flow dynamics lies in the process of turbulent eddies being sheared by flows of a larger scale. This shearing mechanism plays a vital role in diminishing turbulence and associated transport.

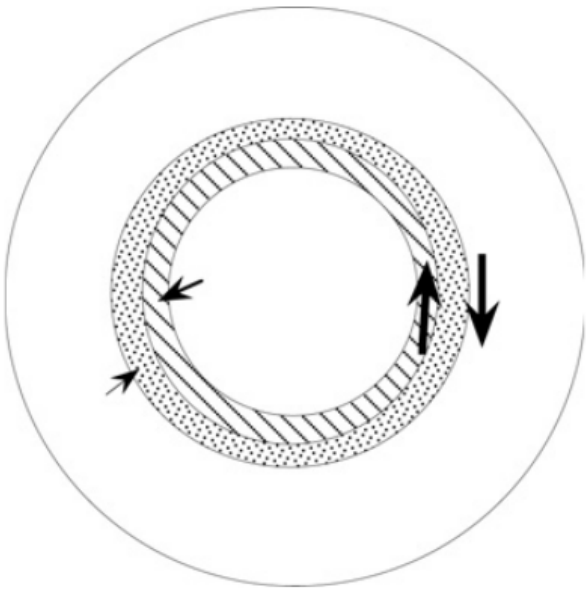

Figure 3.8. Zonal flows within a tokamak from a poloidal cross-section. The hatched area signifies positive charge, while the dotted region represents negative charge, the prominent large arrows provide insight into the flow direction. Source: (Diamond et al., 2005)

According to Numata et al. (2007), the transition from the turbulent to the zonal flow regime can be explained by calculating the ratio between the kinetic energy of the zonal flow (K_Z) and the total kinetic energy (K_T). Thus, the energy of zonal flows is given by

$$K_Z = \frac{1}{2} \int \left(\frac{\partial \langle \varphi \rangle_y}{\partial x} \right)^2 dx, \tag{3.40}$$

where $\langle \varphi \rangle_y$ represent the average of φ in the y direction. The total kinetic energy by

$$K_T = \frac{1}{2} \int |\nabla \varphi|^2 \, dx. \tag{3.41}$$

3.4 Hasegawa-Wakatani Model

The Hasegawa-Wakatani equations provide a simplified model depicting the behavior of drift wave turbulence within the edge region of a tokamak. This model takes into account a magnetically confined plasma and a non-uniform background density gradient ∇n_0 (Hasegawa and Wakatani, 1983; Wakatani and Hasegawa, 1984).

Based on experimental observations, as indicated by Dewhurst (2010) it is apparent that fluctuations within the edge region of numerous magnetically confined plasma closely resemble electrostatic phenomena. Consequently, for the Hasegawa-Wakatani (HW) model, the assumption is made that electric fields $\vec{E}$ can be described in relation to an electrostatic potential φ, thus $E = -\nabla\varphi$.

Assume that the ions are considered cold for simplification purposes, $T_i = 0$, and the plasma is isothermal with $T_e = T = constant$. The electron inertia is neglected due to the electron's

significantly smaller mass in comparison to the ion. In addition, all of the viscosity terms for the anisotropic pressure tensor are ignored and quasineutrality is assumed, where $n_e = n_i = n$.

The derivation of the Hasegawa-Hakatani equations is done as described by Dewhurst (2010) in his PhD thesis (See Dewhurst, 2010, pp. 56–61) . Thus, applying the above assumptions, we start from the equation of motion of the ions in the direction perpendicular to the magnetic field, which has the following form:

$$m_i n \left(\frac{\partial}{\partial t} + \vec{v}_i \cdot \nabla_\perp \right) \vec{v}_i = ne(-\nabla_\perp \varphi + \vec{v}_i \times \vec{B}), \tag{3.42}$$

where m_i is the ion mass and $\vec{v}_i$ is the ion velocity.

The lowest-order ion perpendicular velocity is determined by equating the left-hand side to zero and subsequently performing a cross product with B, resulting in the $\vec{E} \times \vec{B}$ drift velocity.

$$\vec{v}_E = \frac{\vec{B} \times \nabla_\perp \varphi}{B}, \tag{3.43}$$

where $B = |\vec{B}|$. By substituting $\vec{v}_E$ into the momentum equation and taking the cross product with B, we obtain the polarization drift velocity.

$$\vec{v}_p = \frac{m_i}{eB} \vec{B} \times \left(\frac{\partial}{\partial t} + \vec{v}_E \cdot \nabla_\perp \right) \vec{v}_E, \tag{3.44}$$

Therefore, the ion perpendicular equation of motion is simplified to a velocity equation

$$\vec{v}_{i\perp} = \vec{v}_E + \vec{v}_p, \tag{3.45}$$

$$\vec{v}_{i\perp} = \frac{\vec{B} \times \nabla_\perp \varphi}{B} + \frac{m_i}{eB} \vec{B} \times \left(\frac{\partial}{\partial t} + \vec{v}_E \cdot \nabla_\perp \right) \vec{v}_E. \tag{3.46}$$

Similarly, the equation of motion for electrons perpendicular to a magnetic field is expressed as a velocity. The electron perpendicular equation of motion is given by

$$0 = -ne(-\nabla_\perp \varphi + \vec{v}_e \times B) - T \nabla_\perp n. \tag{3.47}$$

Thus, for the electron perpendicular velocity taking the cross product

$$\vec{v}_{e\perp} = \frac{\vec{B} \times \nabla_\perp \varphi}{B} - \frac{\vec{B} \times T \nabla_\perp n}{neB}, \tag{3.48}$$

$$\vec{v}_{e\perp} = \vec{v}_E + \vec{v}_{de}, \tag{3.49}$$

$\vec{v}_{de}$ is the electron diamagnetic drift velocity. It is important to note that the polarization drift of electrons is not considered because of their small mass, and for the ions, the diamagnetic drift is neglected under the assumption that $T_i = 0$.

After establishing the equations of motion perpendicular to the magnetic field for particles, we will now investigate their motion in the parallel direction. The parallel dynamics is controlled

by the electrons due to the electron/ion mass ratio that only considers the movements of the electrons, assuming a stationary character for the ions, that is, $v_{i\parallel} = 0$. Hence the parallel electron equation of motion is described how

$$0 = ne\nabla_{\parallel}\varphi - T\nabla_{\parallel}n - \eta e^2 n^2 \vec{v}_{e\parallel}, \tag{3.50}$$

being η is the resistivity, the term $\eta e^2 n^2 \vec{v}_{e\parallel}$ is responsible for models the collisions between the particles. If $\eta = 0$ the equation would lead to adiabatic electron response, therefore, there be no drift wave instability. Rewriting the Equation (3.50) in function of parallel current density, we get

$$\vec{J}_{\parallel} = \frac{T}{e\eta}\left[\frac{\nabla_{\parallel}n}{n} - \frac{e\nabla_{\parallel}\varphi}{T}\right]. \tag{3.51}$$

In this context, we can obtain the Hasegawa-Wakatani equations from the Branginskii continuity equations by associating the motion of particles and their velocities (Braginskii, 1965). The electron continuity equation is given by

$$\frac{\partial n}{\partial t} + \vec{v}_{e\perp}\cdot\nabla_{\perp}n + n\nabla_{\perp}\cdot\vec{v}_{e\perp} - \frac{1}{e}\nabla_{\parallel}\cdot\vec{J}_{\parallel} = 0, \tag{3.52}$$

considering that $\nabla_{\perp}\cdot\vec{v}_E = 0$, $\nabla_{\perp}\cdot\vec{v}_{de} = 0$, $\vec{v}_{de}\cdot\nabla_{\perp}n = 0$. Assuming $\vec{v}_{e\perp} = \vec{v}_E + \vec{v}_{de}$, (3.49), we get

$$\left(\frac{\partial}{\partial t} + \vec{v}_E\cdot\nabla_{\perp}\right)n - \frac{1}{e}\nabla_{\parallel}\cdot\vec{J}_{\parallel} = 0. \tag{3.53}$$

For the ions, the continuity equation is

$$\frac{\partial n}{\partial t} + \vec{v}_{i\perp}\cdot\nabla_{\perp}n + n\nabla_{\perp}\cdot\vec{v}_{i\perp} = 0, \tag{3.54}$$

where $\vec{v}_{i\perp} = \vec{v}_E + \vec{v}_p$, $\nabla_{\perp}\cdot\vec{v}_E = 0$ and neglecting the nonlinear term $\vec{v}_p\cdot\nabla_{\perp}n$. The equation becomes

$$\left(\frac{\partial}{\partial t} + \vec{v}_E\cdot\nabla_{\perp}\right)n + n\nabla_{\perp}\cdot\vec{v}_p = 0. \tag{3.55}$$

Due to quasi-neutrality, the equations for the continuity of electrons and ions, (3.53) and (3.55), can be equated, leading to

$$n\nabla_{\perp}\cdot\vec{v}_p = -\frac{1}{e}\nabla_{\parallel}\cdot\vec{J}_{\parallel}, \tag{3.56}$$

knowing that $\vec{v}_p$ is given by (3.44), the term $\nabla_{\perp}\cdot\vec{v}_p$ can be written as

$$\nabla_{\perp}\cdot\vec{v}_p = -\frac{m_i}{e}\frac{1}{B^2}\left(\frac{\partial}{\partial t} + \vec{v}_E\cdot\nabla_{\perp}\right)\nabla^2\varphi, \tag{3.57}$$

thus, the Equation (3.56) is rewritten as

$$\left(\frac{\partial}{\partial t} + \vec{v}_E\cdot\nabla_{\perp}\right)\nabla^2\varphi = \frac{B^2}{nm_i}\nabla_{\parallel}\cdot\vec{J}_{\parallel}, \tag{3.58}$$

being $\nabla^2\varphi$ the vorticity. This leads to the three-dimensional Hasegawa-Wakatani equations that can be reduced to two spatial dimensions (Hasegawa and Mima, 1978). Therefore, the variables are separated into background and fluctuating components $n = n_0 + \tilde{n}$, where $n_0 \gg \tilde{n}$, $\partial n_0/\partial t = 0$ and $\nabla_\parallel n_0 = 0$.

Considering the background density is zero, i.e. $\varphi = \tilde{\varphi}$, the equation for parallel current density described by (3.51) can be written by

$$\vec{J}_\parallel = \frac{T}{e\eta}\left[\frac{\nabla_\parallel \tilde{n}}{n_0} - \frac{e\nabla_\parallel \tilde{\varphi}}{T}\right]. \tag{3.59}$$

For the two-dimensional model, a single parallel wavenumber k - characteristic of the fluctuations of the drift waves along the magnetic field lines in the toroidal direction - is assumed, whereby $\nabla_\parallel^2 = -k^2$, thus, the divergence of $J_\parallel$ is given by

$$\nabla_\parallel \cdot \vec{J}_\parallel = \frac{Tk^2}{e\eta}\left[\frac{e\tilde{\varphi}}{T} - \frac{\tilde{n}}{n_0}\right]. \tag{3.60}$$

In the reference geometry, the magnetic field is oriented in the z-direction, denoted as $\vec{B} = \hat{z}$, and there exists a background density gradient along the negative x-direction, given by $\nabla n_0 = -\hat{x}n_0/L_n$, with L_n representing the length scale of the gradient. Consequently, the x and y directions can be associated with the radial and poloidal directions, respectively, within a tokamak.

The nonlinear terms can be expressed utilizing the Poisson bracket notation as

$$\vec{v}_E \cdot \nabla_\perp = \frac{1}{B}\left[\,\tilde{\varphi},\right], \tag{3.61}$$

the notation being described by

$$[A, B] = \frac{\partial A}{\partial x}\frac{\partial B}{\partial y} - \frac{\partial A}{\partial y}\frac{\partial B}{\partial x}. \tag{3.62}$$

For the normalization of equations we can use the following non dimensional variables

$$\frac{e\tilde{\varphi}}{T} \equiv \varphi,\ \frac{\tilde{n}}{n_0} \equiv n,\ \omega_c t \equiv t,\ \frac{x}{\rho_s} \equiv x, \tag{3.63}$$

being ω_c is the ion cyclotron frequency and $\rho_s = \sqrt{m_i T/eB}$ is the hybrid Larmor radius. As a result, the Hasegawa-Wakatani equations can be expressed by

$$\frac{\partial}{\partial t}\zeta + [\varphi, \zeta] = \alpha\,(\varphi - n) - D\nabla^4\zeta, \tag{3.64}$$

$$\frac{\partial}{\partial t}n + [\varphi, \zeta] = \alpha\,(\varphi - n) - \kappa\frac{\partial \varphi}{\partial y} - \nabla^4 n, \tag{3.65}$$

being ζ is the vorticity, D is the dissipation coefficient, and κ characterizes the background

density gradient which drives the system and is represented by

$$\kappa = -\frac{\partial \ln n_0}{\partial x}, \tag{3.66}$$

with regards to α, the parameter controls the strength of the resistive coupling between n and φ through the parallel current. The adiabaticity parameter dictates the extent to which electrons can rapidly move along magnetic field lines and establish a perturbed Boltzmann density response (Anderson and Hnat, 2017). The α parameter is given by

$$\alpha = \frac{Tk^2}{n_0 e^2 \eta \omega_c}, \tag{3.67}$$

when $\alpha \to \infty$ (adiabatic limit) and $n \to \varphi$ the density fluctuations are strongly associated with electrostatic potential fluctuations, the Hasegawa-Wakatani equations transform into an equivalent form, resembling the one-field, indirectly forced Charney-Hasegawa-Mima equation (Hasegawa and Mima, 1978).

When $\alpha \to 0$ is called hydrodynamic limit, the equations are decoupled and is equivalent to the incompressible Euler equation in 2D being the vorticity is determined by 2D Navier-Stokes equation. Additionally, for non-zero α , there is a growth rate that induces random stirring, preventing the vorticity from decaying to zero. According to Anderson and Hnat (2017), this deviates from the typical behavior observed in the unforced Navier-Stokes equation.

3.4.1 Modified Hasegawa-Wakatani Model

In tokamaks, it has been observed that the zonal components of the potential and density do not contribute to the parallel current, since the zonal fluxes are considered damped in the Hasegawa-Wakatani equations described in Section 3.4 (Dewhurst, 2010). The modified Hasegawa-Wakatani equations, are obtained by removing the zonal components from the parallel coupling terms enabling the self-generation of zonal flows. Thus, the Equations (3.64), (3.65) can be rewritten as

$$\frac{\partial}{\partial t}\zeta + [\varphi, \zeta] = \alpha\left(\widetilde{\varphi} - \widetilde{n}\right) - D\nabla^4\zeta, \tag{3.68}$$

$$\frac{\partial}{\partial t}n + [\varphi, \zeta] = \alpha\left(\widetilde{\varphi} - \widetilde{n}\right) - \kappa\frac{\partial \varphi}{\partial y} - \nabla^4 n, \tag{3.69}$$

where the zonal and non-zonal components of φ, n are given by

$$zonal : \langle\varphi\rangle \equiv \frac{1}{L_y}\int \varphi dy,\ \langle n\rangle \equiv \frac{1}{L_y}\int n dy, \tag{3.70}$$

$$non - zonal : \tilde{\varphi} \equiv \varphi - \langle\varphi\rangle,\ \tilde{n} \equiv n - \langle n\rangle. \tag{3.71}$$

The square brackets $\langle ... \rangle$ denotes an average in the poloidal direction, and $\tilde{\varphi}$, $\tilde{n}$ represent the fluctuating in with the surface averaged component removed, i.e. the turbulent parts of the total fluctuating fields φ, n.

From the Equations (3.68)-(3.69) for electrostatic potential the velocity field is defined by

$$v_x \equiv -\frac{\partial \tilde{\varphi}}{\partial y}, \quad v_y \equiv -\frac{\partial \tilde{\varphi}}{\partial x}. \tag{3.72}$$

This chapter concludes the presentation of the theoretical background, in which the physical fundamentals necessary for a proper understanding of this work have been presented, from the definition of the plasma to its application in nuclear fusion and its behavior in confinement. The acquired knowledge has been applied to the necessary analysis tools, as explained in subsequent chapters.

4 Analysis Tools

4.1 Modified Hasegawa-Wakatani Model

The modified Hasegawa-Wakatani equations, (3.68)-(3.69), were implemented in Fortran 90 and solved using the finite difference method for spatial derivatives and the fourth-order Runge-Kutta method for integration over time. The Poisson brackets were tackled utilizing the Arakawa method that conserves energy and entropy with third-order accuracy.

The equations were discretized on a 256×256 $2D$ spatial grid, ensuring accurate solutions and reasonable computing time. The initial conditions comprise of small amplitude random noise. Parameters D and κ were respectively assigned values of 10^{-4} and 10^{-1}, being α was chosen as a control parameter. Solving equations (3.68)-(3.69) needed 10^8 time steps to achieve a steady-state solution.

4.2 Fourier Transform

Spectral analysis, or Fourier analysis, is a statistical technique used to analyze time series data using Fourier analysis methods. These methods consist of series and transforms first introduced by the French mathematician and physicist Jean-Baptiste Joseph Fourier in the 18th century during his studies on heat diffusion and propagation phenomena (Carslaw, 1930; Oppenheim et al., 1997; Aguirre, 1995).

The Fourier transform normally uses a time series or a continuous function in the time domain and transforms it into a frequency spectrum, in other words, it converts a function from the time domain to the frequency domain, decomposing the function into sinusoids of different frequencies (Press, 2007; Aguirre, 1995). The function that makes this change of domain possible is called the analysis equation, or Fourier integral, and is given by

$$X(\omega) = \int_{-\infty}^{+\infty} x(t) e^{i\omega t} dt, \tag{4.1}$$

where $i = \sqrt{-1}$ and $\omega = 2\pi f$. Thus, to obtain the inverse function, that is, the origin function in the time domain from the function given in the frequency domain without losing any information, the synthesis equation, or inverse Fourier transform, is utilized. This equation is expressed as:

$$x(t) = \frac{1}{2\pi} \int_{-\infty}^{+\infty} X(\omega) e^{-i\omega t} d\omega. \tag{4.2}$$

For discrete domain, integrals give way to summation. Therefore, we can rewrite Equations (4.1)-(4.2) as follows:

$$X(\omega) = \frac{1}{M} \sum_{t=0}^{M-1} x(t) e^{-i\omega t/M} \tag{4.3}$$

$$x(t) = \frac{1}{M} \sum_{t=0}^{M-1} X(\omega) e^{i\omega t/M} \tag{4.4}$$

Transforms are not limited to temporal frequencies and time domain functions, they are also applicable in analyzing spatial frequencies. Thus, for the Fourier transform of a 1D scalar field u(x,t), we have

$$u(x,t) = \frac{1}{M} \sum_{k=0}^{M-1} \hat{u}(k,t) e^{i2\pi t k_x x/M}, \tag{4.5}$$

where $\hat{u}(t)$ represents the complex Fourier coefficient and for each coefficient there is an amplitude define to $|\hat{u}_k(t)| = \sqrt{Re\{\hat{u}_k(t)\}^2 + Im\{\hat{u}_k(t)\}^2}$.

For images, which can be regarded as a two-dimensional signal in the spatial domain, the two-dimensional implementation of Fourier transforms is necessary, thus, the Equation (4.5) becomes

$$u(x,y,t) = \frac{1}{MN} \sum_{k_x=0}^{M-1} \sum_{k_y=0}^{N-1} \hat{u}(k_x k_y, t) e^{i2\pi t \left(\frac{k_x x}{M} + \frac{k_y y}{N}\right)} \tag{4.6}$$

From the Fourier transformation we can obtain the power spectrum that will provide the power distribution of the signal among different frequencies, therefore, revealing the existence of periodic patterns or correlation structures, which is a crucial information for characterizing the signal (Aguirre, 1995; Vaseghi, 2000).

In summary, as mentioned by Vaseghi (2000), signals that have higher correlation or predictability exhibit a more concentrated power spectrum, while signals that are more random or unpredictable tend to display a more dispersed power spectrum. Thus, by analyzing the power spectrum of a signal, we can identify the presence of repetitive structures or correlated patterns. In the following section we will use this tool to explain the concept of spectral entropy.

4.3 Spectral Entropy

In this work we seek to characterize the L-H transition through the spectral entropy, or Shannon entropy, which can be defined in the context of information theory as the quantization of the information contained in a message, relating it to the occurrence of groups of transmitted symbols (Shannon, 1948). This information entropy can be written as a probabilistic function described by

$$H = -\sum_{i=1}^{n} P(x_i) \log_2 P(x_i) \tag{4.7}$$

where $P(x_i)$ is the probability of occurrence of an event associated with a set x of n events.

Applying to the present context, spectral entropy measures the degree of spatial disorder, with the propagation of the energy of the system being reflected in the increase of this disorder (Xi and Gunton, 1995; Rempel et al., 2007). Thus, the spectral entropy for one dimension is given by

$$S(t) = -\sum_{k=1}^{N} p_{k,t} \ln p_{k,t}, \tag{4.8}$$

where $p_{k,t}$ is the relative Fourier weight of the spatial mode k in the power spectrum, which is represented by

$$p_{k,t} = \frac{|\hat{u}(k,t)|^2}{\sum_k |\hat{u}(k,t)|^2} \tag{4.9}$$

being $u(k,t)$ is a real function obtained from Fourier transforms, vide Section 4.2. Normalizing Equation 4.9 we infer that $p_{k,t} \in [0,1]$ and $\sum_{k=1}^{N} p_{k,t} = 1$. We can conclude that entropy will be maximum when $p(k,t) = 1/N$, that is, when the distribution is uniform, in wich case $S(t) = \ln N$ (Badii and Politi, 1997). Thus, the normalized Shannon entropy is given by

$$H(t) = \frac{S(t)}{\ln N}. \tag{4.10}$$

For two-dimensional analysis, the Equation (4.8) is analogous to

$$S(t) = -\sum_{k_x=1}^{M} \sum_{k_y=1}^{N} p_{k_x k_y,t} \ln p_{k_x k_y,t}, \tag{4.11}$$

and the Fourier weight can be rewritten as

$$p_{k_x k_y,t} = \frac{|\hat{u}(k_x k_y,t)|^2}{\sum_{k_x=1}^{M} \sum_{k_y=1}^{N} |\hat{u}(k_x k_y,t)|^2}. \tag{4.12}$$

To better illustrate the concept, figure 4.1 shows two opposite cases, a sinusoidal wave and a random noise. Figure *a*) shows the plot of a sinusoidal function, while in *b*) depicts its power spectrum acquired through Fourier transform. The signal exhibits order and occupies only a narrow frequency band, as demonstrated by the magnitude peak $X(\omega) = 1$ in the power spectrum. This indicates the presence of structure and predictability in the signal, allowing it to conclude that the Shannon entropy is minimum, i.e., $H = 0$. Fig. c) displays a signal with noise characteristics. In d), a uniform distribution in the power spectrum is evident where the signal is characterized by numerous frequencies, indicating the lack of structure in the signal. As a result, the entropy is maximum, and, therefore, $H = 1$.

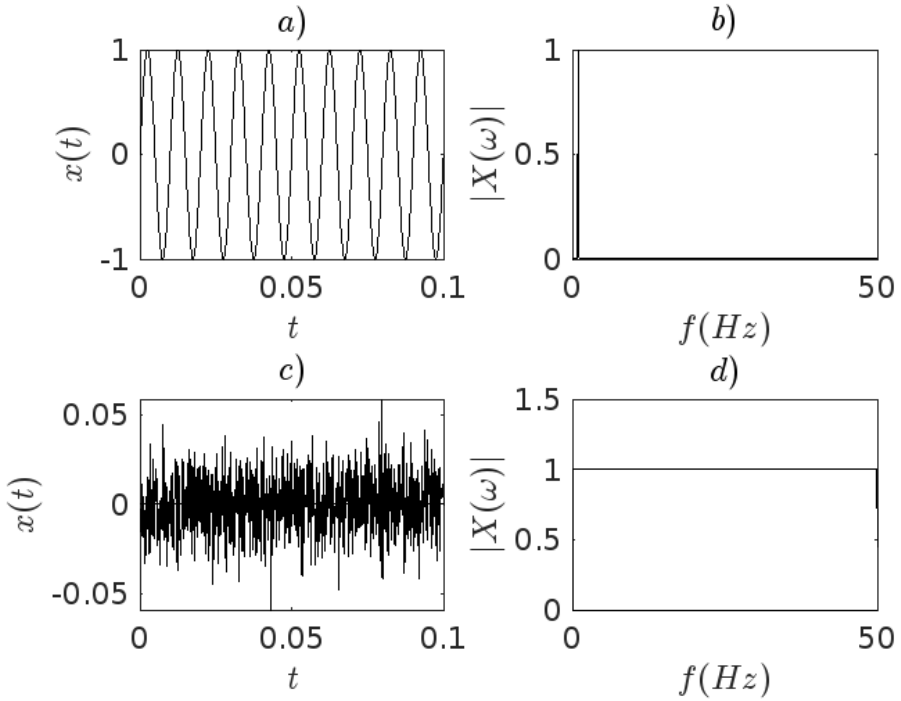

Figure 4.1. Representation of the maximum and minimum values of spectral entropy for a sinusoidal signal in *a*) and a noise in *c*), with their respective power spectra, *b*) and *d*).

The calculation of spectral entropy in 2D, as defined by Equation (4.11), was coded in the C programming language. The Fastest Fourier Transform in the West (FFTW) library was utilized to perform the Fourier transform.

FFTW is a C subroutine library created at the Massachusetts Institute of Technology (MIT) for to calculate the discrete Fourier transform in one or more dimensions, comprising arbitrary input sizes as well as real and complex data, besides data even and odd (discrete transforms of cosines and sines) (Frigo and Johnson, 2005).

This library is based on the so-called fast Fourier transform (FFT) developed by Cooley and Tukey (1965) at IBM. This algorithm reduces the computational time in the order N^2 to $N(\log_2 N$ with N being the number of elements.

4.4 Wavelet Transform

Wavelet transforms arose through the collaborative work of Grossman and Morlet (1985) in the analysis of seismic signals, in which they saw the need for a better representation of signals and images characterized by abrupt changes than those provided by Fourier analysis(Meyer et al., 1992; Farge, 1992).

In Fourier analysis, the transform provides a frequency spectrum for the entire time interval of the analyzed signal, making it ideal for analyzing stationary signals. Nonetheless, for non-stationary signals with varying power spectra, the signal information tends to spread out, which can make it indistinguishable from possible computational noise (Farge, 1992).

To enhance this technique, Gabor (1946) proposed modifications in the Fourier transforms to analyze small signal portions over a specified time interval, which resulted in the development of the windowed Fourier transform or short-time Fourier transform. This method employs an observation window that moves across the time domain, and at each location, the Fourier transform is computed for the signal segment that lies within the window. Although, once the window size is defined, it remains constant for all signal frequencies, which makes local frequency analysis difficult (Daubechies, 1990; Bianchi, 2006).

In this way, wavelets can be understood as an application of the windowed Fourier transform to regions of variable dimensions. In contrast to the Fourier Transform, wavelets are based on functions of compact support, that is, limited duration. This means that these functions are nonzero only to a finite extent and equal to zero everywhere else. This characteristic makes wavelets particularly useful in image analysis, as they allow more effective detection of changes in regions or edges of the image (Meyer et al., 1992; Bianchi, 2006).

Through the wavelet transforms, a signal, or field, can be decomposed into function bases both in space and in scale, at different levels of resolution. This method provide a time-scale description enabling local analysis of the signal (Farge, 1992). The scale decomposition results from of the dilation or contraction of wavelets, which are analysis functions located in space and given by

$$\psi_{a,b}(t) = \frac{1}{\sqrt{|a|}}\psi\left(\frac{t-a}{a}\right), \quad a, b, \in \mathbb{R}, \tag{4.13}$$

where $a \neq 0$, represent the scale parameter (contraction/dilation), b correspond to displacement parameter, and $\psi(t) \in L^2(\mathbb{R})$ is the generating function, called the mother wavelet. This function must satisfy the admissibility condition, such that $\int \psi(t)dt = \Psi(0) = 0$, and be limited in time and frequency.

After obtaining the generating function, the windowed transform is used, whose window function is a translation/compression in time/frequency of the mother wavelet. Thus, the continuous wavelet transform for a signal $u(t)$ can be described by

$$W_{a,b}(t) = \int_{-\infty}^{\infty} u(t)\psi_{a,b}(t)dt. \tag{4.14}$$

For the discrete domain, the multiresolution analysis (MRA) developed by Mallat (1989) is used, in which the decomposition of signals or images occurs at different resolution scales, allowing the analysis of information at multiple levels of detail. Thus, we have the following scaling relation in discrete time, for the scaling function $\varphi(x)$ and the mother wavelet $\psi(x)$, both $\in L^2(\mathbb{R})$:

$$\varphi(n) = \sum_{i=0}^{N-1} h(i)\varphi(2n-i) \tag{4.15}$$

$$\psi(n) = \varphi(n) = \sum_{i=0}^{N-1} g(i)\varphi(2n-i) \tag{4.16}$$

being g a discrete high-pass filter and h a discrete low-pass filter. Both filters are related to each

other as follows

$$g(n) = h(2N - 1 - n). \tag{4.17}$$

Wavelets are widely recognized for their importance in signal processing, especially in the context of one-dimensional piecewise continuous functions, where they provide optimal approximations. However, their effectiveness diminishes in higher dimensions (Kutyniok and Labate, 2012; Labate et al., 2005).

According to Labate et al. (2005) this becomes apparent when attempting to depict natural images using a 2D wavelet basis. The spatial dispersion of edges results in non-sparse representations, requiring a large number of coefficients for accuracy. To address this problem, several new approaches have been introduced, such as directional wavelets, complex wavelets, ridgelets, curvelets, and contourlets (Labate et al., 2005).

These approaches share the fundamental principle that in order to effectively represent multidimensional functions featuring spatially dispersed discontinuities, the fundamental elements must a greater diversity of shapes and directions compared to classical wavelet bases (Labate et al., 2005). One of these alternative approaches to the construction of an efficient representation of multivariable functions are the so-called shearlets, developed by Labate et al. (2005), which are obtained by dilations, shear transformations, and translations to a generating function (Labate et al., 2005; Guo et al., 2006; Kutyniok and Labate, 2012). As will be better explained below.

4.4.1 Shearlet Transform

Shearlet transforms represent a sophisticated approach to multiscale, multidirectional analysis, specifically designed for extracting information from signals and images characterized by anisotropic structures and preferred orientations. These transforms are particularly relevant to accurate detection of edges, textures, and elongated structures (Labate et al., 2005; Kutyniok and Labate, 2012).

Shearlets stand out due to their anisotropic scaling operator, which elongates one direction more than the other, resulting in heightened directional sensitivity within high-frequency shearlets. To address this, a third operator with rotation-like properties is introduced, allowing for the adjustment of the orientation of generating function. In the shearlet framework, this specific operator is referred to as the shear operator, from which the name "shearlet" originates (Duflot et al., 2019).

Thus, considering a 2D image $f(x, y)$, its shearlet transform can be obtained by anisotropically dilating, shifting, and shearing a basis of generating functions (Labate et al., 2005; Guo et al., 2006; Kutyniok and Labate, 2012). Shearlets 2D are represented using affine systems in $L^2(\mathbb{R}^2)$. For generating function $\psi(x)$, the continuous shearlet system can be defined by

$$\mathcal{SH}(\psi) = \{\psi_{a,s,t}(x) = T_t D_{M_{as}} \psi(x) : a \in \mathbb{R}^+, s \in \mathbb{R}, t \in \mathbb{R}^2\} \tag{4.18}$$

where a, s, t are respectively the dilation, shear and translation parameters. T_t is the translation

operator given by

$$T_t\psi(x) = \psi(x-t), \tag{4.19}$$

and $D_{M_{as}}$ is associated to the matrix M_{as} expressed by

$$D_{M_{as}}\psi(x) = |det(M_{as})|^{-\frac{1}{2}}\psi(M_{as}^{-1}x), \tag{4.20}$$

being $M_{as} = A_aS_s$, where A_a is a parabolic scaling matrix, so-called of anisotropic dilation matrix,

$$A_a = \begin{pmatrix} a & 0 \\ 0 & \sqrt{a} \end{pmatrix}. \tag{4.21}$$

This matrix regulates the scale of shearlets through the use of distinct dilation factors along both axes, resulting in a more extended frequency support of shearlets as it moves towards finer scales (Labate et al., 2005). Matrix S_s is called the shear matrix, responsible for controlling the orientation of the shealets, and represented by

$$S_s = \begin{pmatrix} 1 & s \\ 0 & 1 \end{pmatrix}. \tag{4.22}$$

Thus, M_{as} is given by

$$M_{as} = \begin{pmatrix} a & 0 \\ 0 & \sqrt{a} \end{pmatrix}\begin{pmatrix} 1 & s \\ 0 & 1 \end{pmatrix} = \begin{pmatrix} a & \sqrt{a}s \\ 0 & \sqrt{a} \end{pmatrix}. \tag{4.23}$$

Therefore, for the affin system

$$\mathcal{A}_{M_{as}}(\psi) = \mathcal{A}_{a,s,t}(\psi) = \{\psi_{a,s,t}(x) = a^{-3/4}\psi(M_{as}^{-1}(x-t)) : a \in \mathbb{R}^+, s \in \mathbb{R}, t \in \mathbb{R}^2\}, \tag{4.24}$$

the shearlet function becomes

$$\psi_{a,s,t}(x) = a^{-3/4}\psi(M_{as}^{-1}(x-t)) \tag{4.25}$$

and the continuous sherlet transform, for $f(x) \in L^2(\mathbb{R}^2)$ is defined as the function

$$\mathcal{SH}_f(a,s,t) = \langle f, \psi_{a,s,t}\rangle,\ a \in \mathbb{R}^+, s \in \mathbb{R}, t \in \mathbb{R}^2. \tag{4.26}$$

In the discrete transformation, a set number of decomposition scales and shifts are utilized, and the number of orientations depends on the scale, with greater orientations introduced at higher spatial frequencies (Brazhe, 2018; Kutyniok and Labate, 2012). One of the techniques employed in computing discrete shearlets is the fast finite discrete shearlet transfor (FFST), which was created by Häuser and Steidl (2014) and utilized by Brazhe (2018) for developing entropy and complexity metrics.

From this approach, for a square digital image $f \in \mathbb{R}^{N\times N}$, with the functions sampled on a grid $\{(m_1/N, m_2/N) : (m_1, m_2) \in \mathcal{G}\}$, $\mathcal{G} := \{(m_1, m_2) : m_1 = m_2 = 0, \cdots, N-1\}$. Let be

the number of considered scale $j_0 := \lfloor \frac{1}{2} \log_2 N \rfloor$, the discretization of the dilation, shear and translation parameters presented by Häuser and Steidl (2014) are:

$$a_j := 2^{-2j} = \frac{1}{4^j}, \quad j = 0, \cdots, j_0 - 1, \tag{4.27}$$

$$s_{j,k} := k2^{-j}, \quad -2^j \leq k \leq 2^j \tag{4.28}$$

$$t_m := \left(\frac{m_1}{N}, \frac{m_2}{N}\right), \quad m \in \mathcal{G}. \tag{4.29}$$

With these parameters, shearlet is defined as

$$\psi_{j,k,m}(x) := \psi_{a_j, s_{j,k}, t_m}(x) = a^{-3/4} \psi(A_{a_j}^{-1} S_{s_{j,k}}^{-1}(x - t_m)) \tag{4.30}$$

Brazhe (2018) highlights the importance of the presence of scaling factor $a^{-3/4}$ to achieving a uniform distribution of shearlet coefficient power when processing input data consisting of spatially uncorrelated random images. These images, for the present work, are obtained through the numerical implementation of the Hasegawa-Wakatani model for confined plasma.

Therefore, Brazhe (2018) formally defines the shearlet transform as a process that maps an image f to a set of shearlet coefficients. As the translation grid m remains scale-independent and redundant, these shearlet coefficients can alternatively be represented as a series of images $S_{j,k}(x, y)$ sharing the same dimensions as f. Thus, the normalized power of these coefficients can be utilized to depict local feature statistics and relate it to probability density, and consequently, estimate of local entropy and complexity.

4.5 Entropy - Complexity Index

Complexity is defined by López-Ruiz et al. (1995) as the interaction between the information contained within a system and its disequilibrium based on a probabilistic description of a given physical system. The quantization of this information is related to the normalized Shannon entropy $H(t)$, (4.10) presented in section 4.3.

The new concept introduced by this approach is the disequilibrium D, which describes a distance between an observed probabilistic distribution P from an uniform distribution adopted (P_e) (López-Ruiz et al., 1995; Brazhe, 2018). Thus, there is

$$D = \sum_{i-1}^{N} (P_i - 1/N)^2. \tag{4.31}$$

Similarly, as conducted by Rosso et al. (2007) and Miranda et al. (2021), we will utilize the normalized Jensen-Shannon divergence as a measure of disequilibrium, thus

$$Q_{JS} = \frac{J(P, P_e)}{J_{max}}, \tag{4.32}$$

being $J(P, P_e)$ is described by

$$J(P, P_e) = S\left(\frac{P + P_e}{2}\right) - \frac{1}{2}S(P) - \frac{1}{2}S(P_e). \tag{4.33}$$

Consequently, the Jensen-Shannon (J-S) complexity

$$C_J^S = Q_{JS}(P, P_e)H(P) \tag{4.34}$$

According to Miranda et al. (2021) the pair (H, C_J^S) can be graphically represented within the complexity-entropy (C-H) plane. This plane can be divided into three distinct regions: a low-entropy and low-complexity region, which characterizes highly predictable systems; an intermediate-entropy and high-complexity region, representing unpredictable systems with significant structure; and a high-entropy and low-complexity region, indicative of stochastic-like processes (Rosso et al., 2007).

The obtained complexity measure quantifies both the degree of randomness and range of spatial correlations within the data. As a result, a range of acceptable complexity values exist for each entropy value H, with an upper limit of C_{max} and a lower limit of C_{min}, thus giving to the C-H plane its characteristic half-moon shape (Rosso et al., 2007; Brazhe, 2018).

The study utilized the C-H plane construction by (H, C_J^S). The normalized Shannon entropy was obtained from Equation (4.10) and normalized shearlet power coefficients were used as a probabilistic distribution for calculating J-S complexity based on Equation (4.34). A shearlet-based algorithm is used to calculate both variables. The algorithm is publicly accessible on the open-source platform `https://github.com/abrazhe/shearlexity`. The open source software used is based on the fast finite discrete shearlet transform (FFST) (Häuser and Steidl, 2014).

4.6 Bifurcation Diagram

Bifurcation diagrams are classical tools for studying the dynamics of nonlinear systems; they represent the possible behaviors of a dynamic system as a parameter of the model being analyzed is varied (Vaidyanathan et al., 2021; Nusse et al., 1994). In this way, three diagrams were constructed, one for the ratio between the kinetic energy of the zonal flow and the total kinetic energy K_Z/K_T, one related to the normalized Shannon entropy, and finally the Jensen-Shanon complexity index, all as a function of the control parameter α - adiabaticity parameter.

First, to construct the diagrams, the analysis interval for the control parameter was defined with $\alpha_{min} = 10^{-3}$ and $\alpha_{max} = 1$, values determined according to studies carried out by Numata et al. (2007). After that, α was selected in the middle of the range, that is, $\alpha = (\alpha_{max} - \alpha_{min})/2$, for this value we solve the modified Hasegawa-Wakatani equations and store 5000 files containing the electrostatic potential. These 5000 files will be used to compute average values for that value of α. The interval was segmented again to obtain a new value of α, now $\alpha = (\alpha_{max} - \alpha_{min})/4$, the modified Hasegawa-Watakani equations were solved again obtaining new 500 values of φ. After that, α was defined as $\alpha = 3(\alpha_{max} - \alpha_{min})/4$ and once again the simulation of the modified

Hasegawa-Wakatani Equations was executed. We repeat these last two steps to refine the values given to α.

At the end of the simulation, 85,000 files were obtained, 5,000 for each value of α, then the calculations of the mean and variance of the zonal and total energies were performed according to the equations (3.40)-(3.41), entropy (4.11) and complexity (4.34), to then construct their respective bifurcation diagrams.

The methodology described above allows us to recognize the different regimes faster than increasing the control parameter α by a small constant value.

5 Results

Fig. (5.1) illustrates the electrostatic potential pattern, highlighting two distinct regimes. In subfigure (a), representing the turbulent regime ($\alpha = 0.010182$), vortices are evident as regions with local minima and maxima in φ. The potential in this regime appears diffuse without well-defined zones. Subfigure (b) depicts the zonal flow regime ($\alpha = 0.01747$), characterized by prominent zonally elongated structures in the electrostatic potential, which play a dominant role in flow dynamics. Zonal flows have the ability to suppress turbulence and diminish the radial mass flow toward the tokamak walls, thus enhancing plasma confinement. In this model, the transition between these two states is referred to as the L-H confinement transition.

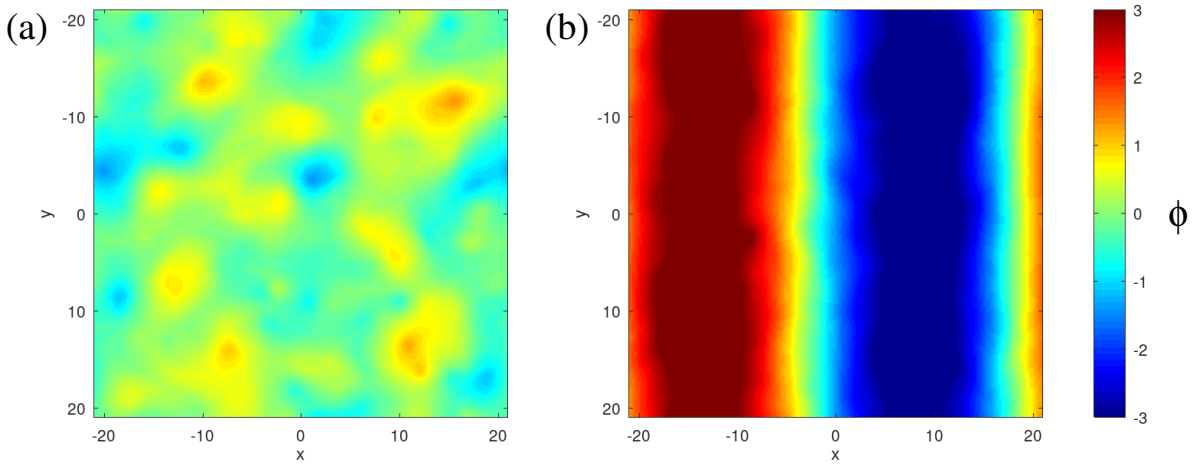

Figure 5.1. Electrostatic potential patterns φ, in (a) the turbulent regime ($\alpha = 0.010182$), and (b) the zonal-flow regime ($\alpha = 0.010747$).

We investigate the L-H confinement transition by constructing a bifurcation diagram, as described in section 4.6. The transition from the turbulent regime to the zonal-flow regime is evident when calculating the ratio of the kinetic energy of the zonal flow K_Z (3.40) to the total kinetic energy K_T (3.41).

In Fig. (5.2), we analyze the transition from the turbulent regime ($\alpha < 0.0103$) to the zonal-flow regime ($\alpha > 0.0103$) and its impact on the electrostatic potential. The upper panel displays the average of 5000 values of K_Z/K_T for a given value of α. In the turbulent regime, K_Z/K_T values are notably low, indicating minimal zonal flow influence. However, as we transition to the zonal-flow regime, K_Z/K_T values approach one, confirming the prevalence of zonal flows. This L-H transition takes place around $\alpha \sim 0.0103$. Error bars in this panel reflect the variability of

kinetic energy, with larger bars in the turbulent regime, signifying more significant fluctuations compared to the zonal-flow regime.

In the lower panel of Fig. (5.2), we show the normalized spectral entropy applied to the electrostatic potential φ for the same range of α values. Spectral entropy provides insight into the degree of order or disorder within the electrostatic potential patterns. In both the turbulent and zonal flow regimes, averaged spectral entropy values are consistently low (less than 0.3), This implies that the electrostatic potential exhibits orderly patterns in both regimes.

Comparing spectral entropy values before and after the L-H transition, we observe that the turbulent regime exhibits higher entropy values than the zonal-flow regime, indicating a higher degree of disorder in the former. This aligns with the role of zonal flows in suppressing turbulence, serving as barriers against horizontal plasma particle flux, and ultimately enhancing plasma confinement.

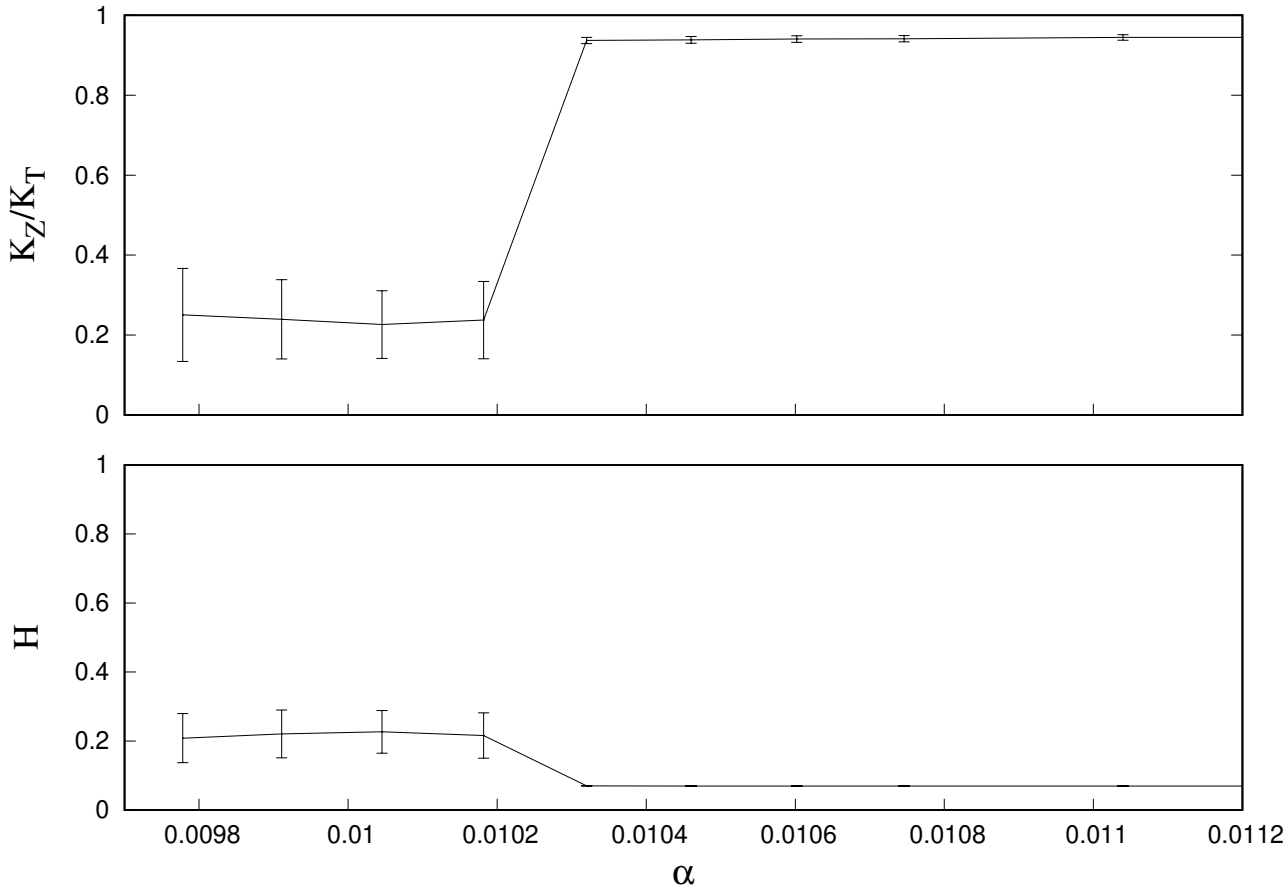

Figure 5.2. Bifurcation diagram of the ratio between the kinetic energy of zonal flows and the total kinetic energy, and the spectral entropy, as a function of the control parameter α.

We conducted a preliminary analysis constructing a bifurcation diagram of the V_x and V_y velocity field components for electrostatic potential for different values of the control parameter, α. Figure (5.3) illustrates that the radial component, V_x, which has a small variation in the transition to zonal flow. This transition is most evident in V_y. Due to the accentuated slope of the poloidal component of the velocity field, denoted by V_y, two distinct scenarios arise in the

behavior of potential. Hence, our investigation will be restricted to this component since it has a significant impact on the course of the electrostatic potential.

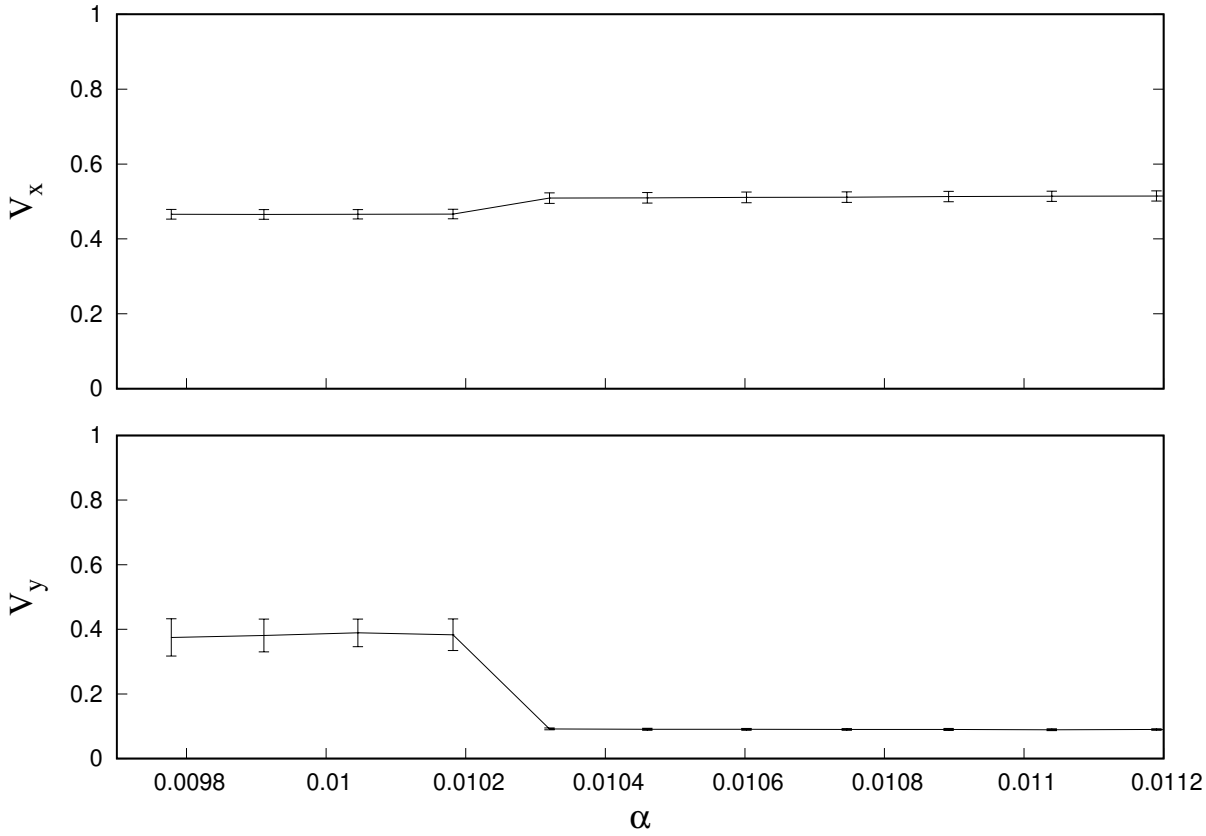

Figure 5.3. Bifurcation diagram of the V_x and V_y velocity field components for electrostatic potential, as a function of the control parameter α.

We delve into the spectral characteristics of the spatial patterns shown in Fig. (5.1) by analyzing the power spectra of the V_y component of the velocity field. To do this, we performed a 2D Fourier transform to obtain the power spectra of V_y. The 2D spectra were then simplified to 1D spectra by calculating the radial mean of the absolute values of the complex Fourier coefficients.

Thus, Fig. (5.4) illustrates the power spectra of the $V_y(x, y, t)$ velocity component for both the turbulent and zonal flow regimes. Each curve represents the average of 20 power spectra computed from various spatial patterns of V_y at different time instances, with the vertical error bars indicating the standard deviation. In this figure, it is evident that the zonal flow regime displays a distinct peak at the lowest wavenumber. This peak is a consequence of the prominent large-scale structure associated with the zonal flow, as depicted in Fig. 1(b).

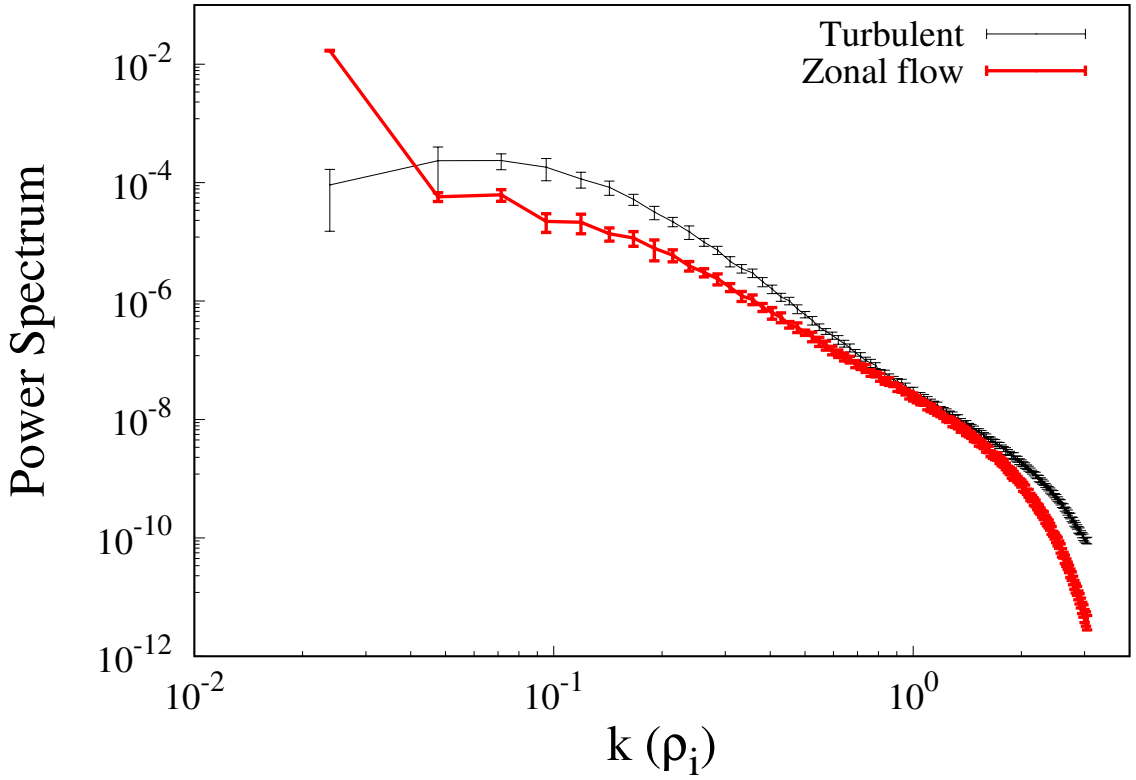

Figure 5.4. The ring-averaged power spectrum of V_y in the turbulent regime (black thin line) and in the zonal flow regime (red thick line). The vertical lines represent the standard deviation of the average of 20 spectra computed at each regime.

For the local analysis of entropy-complexity, we apply the shearlets technique as described in section 4.4.1. First, we applied this technique to a well-known fractal, the Sierpiński carpet. It is constructed from an initial square that is divided into nine subsquares, forming a 3×3 grid, with the central subsquare removed. This is done recursively for the remaining eight subsquares, this process occurs infinitely (Allouche and Shallit, 2003).

The left panel of figure (5.5) shows the Sierpiński carpet obtained after 7 iterations. The middle panel shows the map of local entropy H and the right panel the map of local complexity C. Note that the regions surrounding the largest squares have higher entropy and lower complexity, a result similar to that found for signals characterized by noise. In the regions of the largest squares themselves, we find higher complexity and lower entropy, which can predict the presence of structure in this part of the image. This analysis of the Sierpiński carpet demonstrates that the shearlet technique allows to obtain local values of entropy-complexity, and interpret them in terms of coherent structures in images.

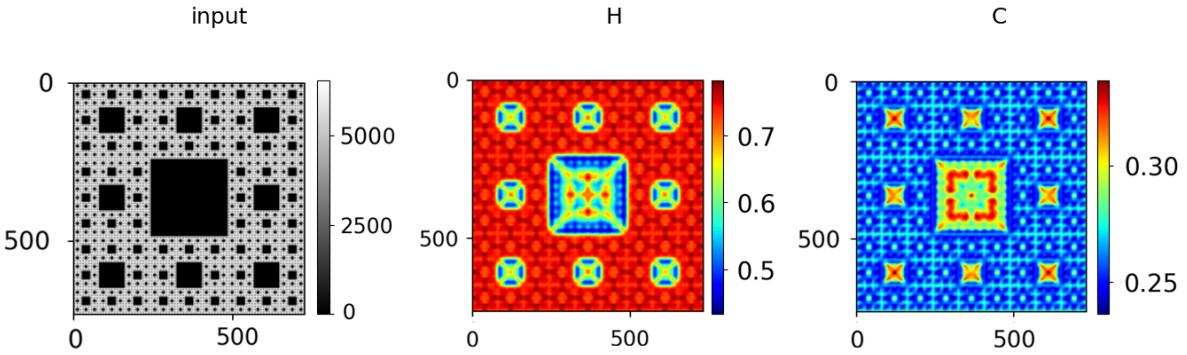

Figure 5.5. The local entropy H (middle) and the local complexity maps (right) for the Sierpiński carpet (left).

The next Figure (5.6) shows the maps of local entropy (H) and local complexity (C_{JS}) for the V_y component of the velocity field in the turbulent and zonal flow regimes. It is worth noting that the color bars for H and C_{JS} in these two regimes are set to the same scale, which facilitates a direct comparison.

Examining Figures 5.6(a) and 5.6(b) in the turbulent regime ($\alpha = 0.010182$), it is observed that regions with localized minimum entropy correspond to high complexity, while regions with elevated entropy values correspond to low complexity. This observation suggests that within the turbulent regime, spatial patterns exhibit high entropy values ($H > 0.75$) and intermediate values of C_{JS}.

In the transition to the zonal flow regime, where $\alpha = 0.010747$, as shown in Figures 5.6(c) and 5.6(d), a similar correspondence between low-H regions and high-C_{JS} regions is evident. In this regime, the dominant spatial patterns have higher complexity values and intermediate entropy values.

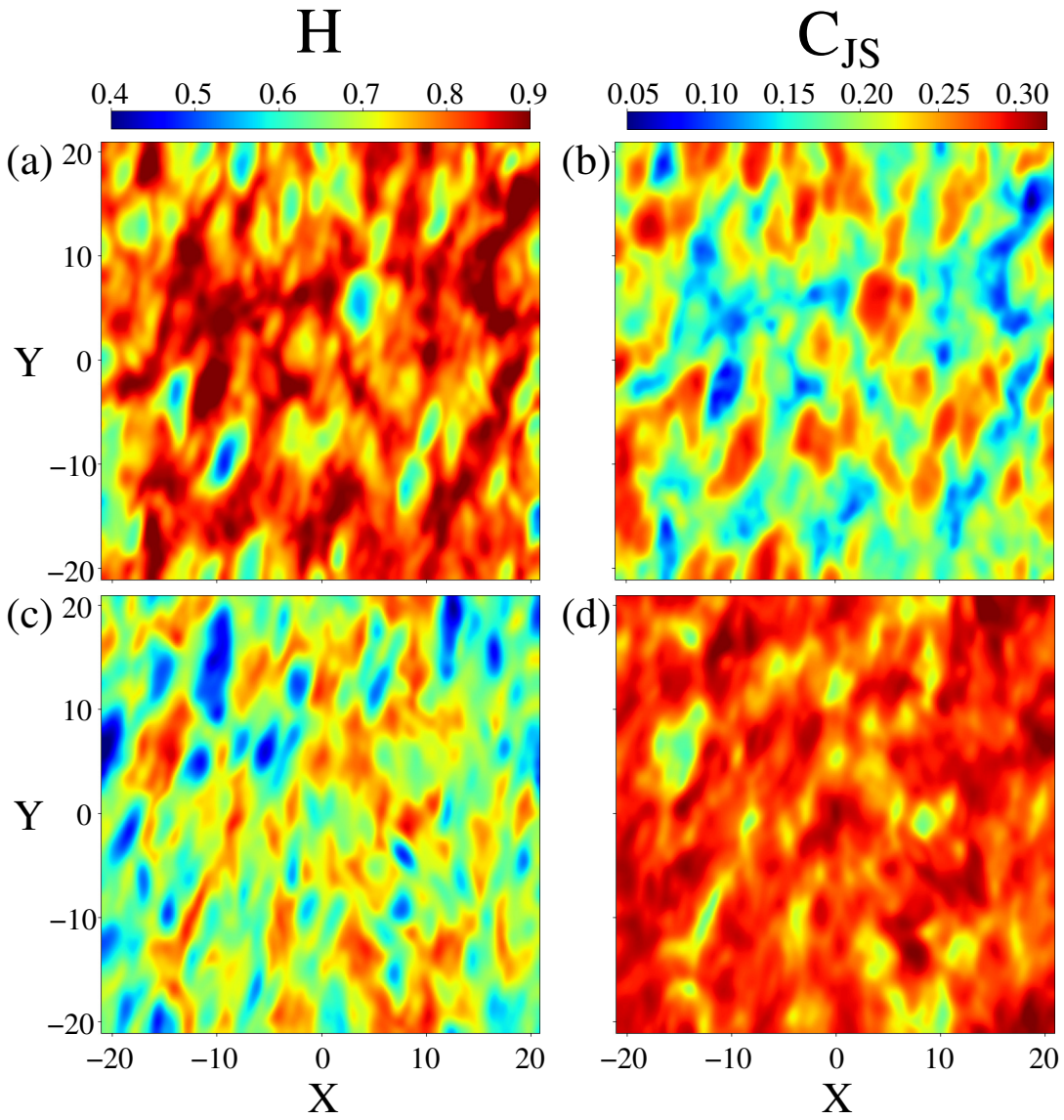

Figure 5.6. (a) The local entropy H and (b) the local complexity C_{JS} maps for the V_y component of the velocity field in the turbulent regime, and (c) the local entropy H and (d) the local complexity C_{JS} maps for the same component of the velocity field in the zonal flow regime.

In Figure 5.7(a), illustrates the averaged values of the ratio between zonal flow kinetic energy and total kinetic energy, represented as K_Z/K_T. The Figure 5.7(b) displays the averaged normalized Shannon entropy H, and the Figure 5.7(c) shows the averaged Jensen-Shannon complexity C_{JS}, all as functions of the adiabaticity parameter α applied to the poloidal component of the velocity field. The vertical bars indicate the standard deviation for each quantity.

In the turbulent regime, K_Z/K_T exhibits low values due to the coexistence of a large number of active modes with zonal flow modes. A significant increase in K_Z/K_T occurs around $\alpha = 0.0103$, marking the transition to a zonal flow-dominated regime, where the majority of energy resides in these modes. This transition results from the suppression of the Kelvin-Helmholtz instability, responsible for disrupting zonal flows and causing energy dispersion, leading to turbulent patterns. Notably, the standard deviation is larger during the turbulent regime than the zonal flow regime, attributed to the poloidal velocity field's large-amplitude fluctuations.

Next, we analyze the global values of entropy-complexity, which are obtained by computing the average of the local values of entropy-complexity over the whole spatial domain, for a given time. The Figure 5.7(b), representing the average normalized Shannon entropy H during the L-H transition, indicates that turbulent patterns exhibit higher entropy compared to the zonal flow regime. This is because the turbulent regime involves kinetic energy spreading among modes, while the zonal flow regime confines energy to a smaller number of modes.

Finally, for Figure 5.7(c), the average Jensen-Shannon complexity C_{JS} demonstrates a transition from lower to higher complexity values. In the zonal flow regime, where most kinetic energy resides in zonal modes, a disequilibrium state is observed. Conversely, the turbulent state involves energy cascading toward smaller scales. As complexity measures the disequilibrium of a system, the zonal flow regime is expected to exhibit a higher degree of complexity compared to the turbulent regime.

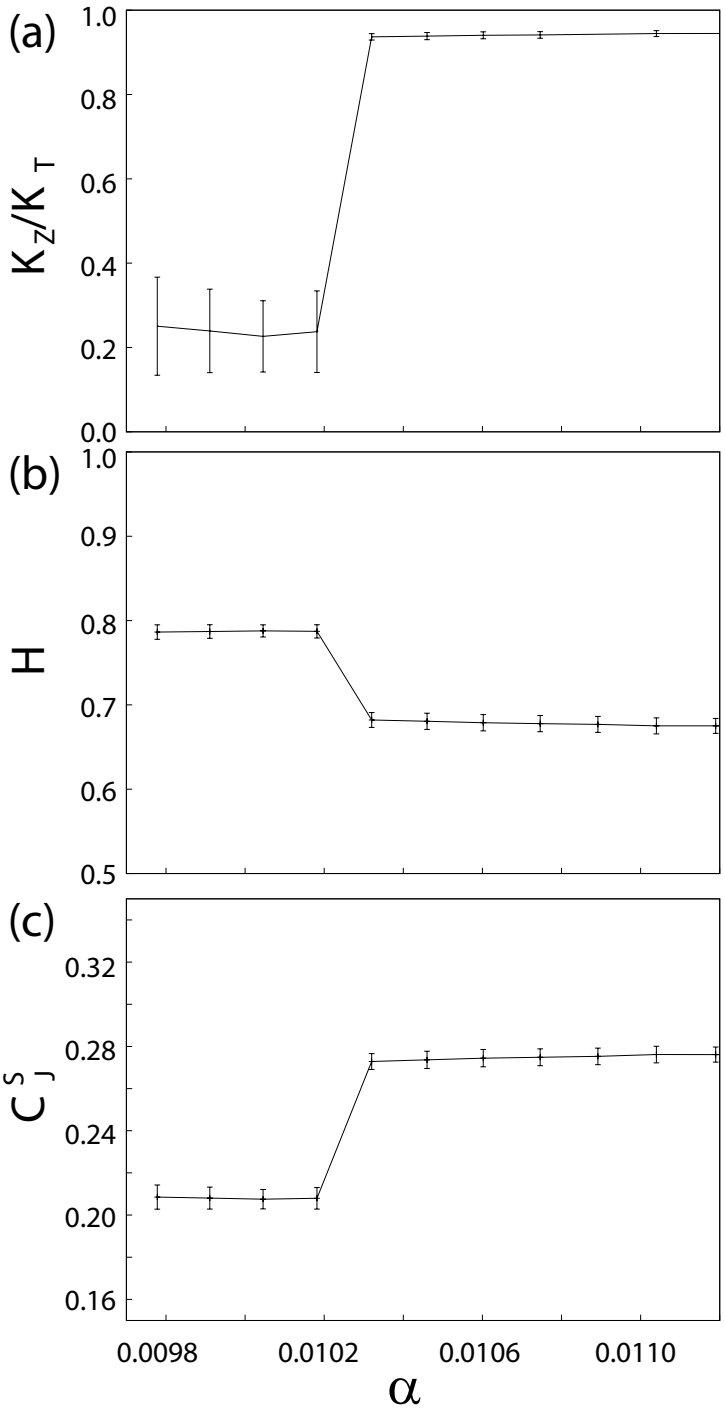

Figure 5.7. Bifurcation diagram of (a) the ratio between the kinetic energy of the zonal flow K_Z, and the total kinetic energy K_T, (b) the normalized Shannon entropy H, and (c) the Jensen-Shannon complexity index (C_J^S), as a function of the control parameter α.

Figure 5.8 illustrates the C-H plane, where the two crescent shaped curves delineate the maximum and minimum values of C_{JS} for a given H. The J-S index of the V_y velocity component in the turbulent regime (represented by crosses) and in the zonal flow regime (represented by plus signs) is shown. The error bars for both H and C_{JS} are smaller than the symbol size. This plot shows that the turbulent regime has a higher degree of entropy and a lower degree of complexity compared to the zonal flow regime. The abrupt change in the J-S index within both the turbulent and zonal flow regimes is evident in the C-H plane.

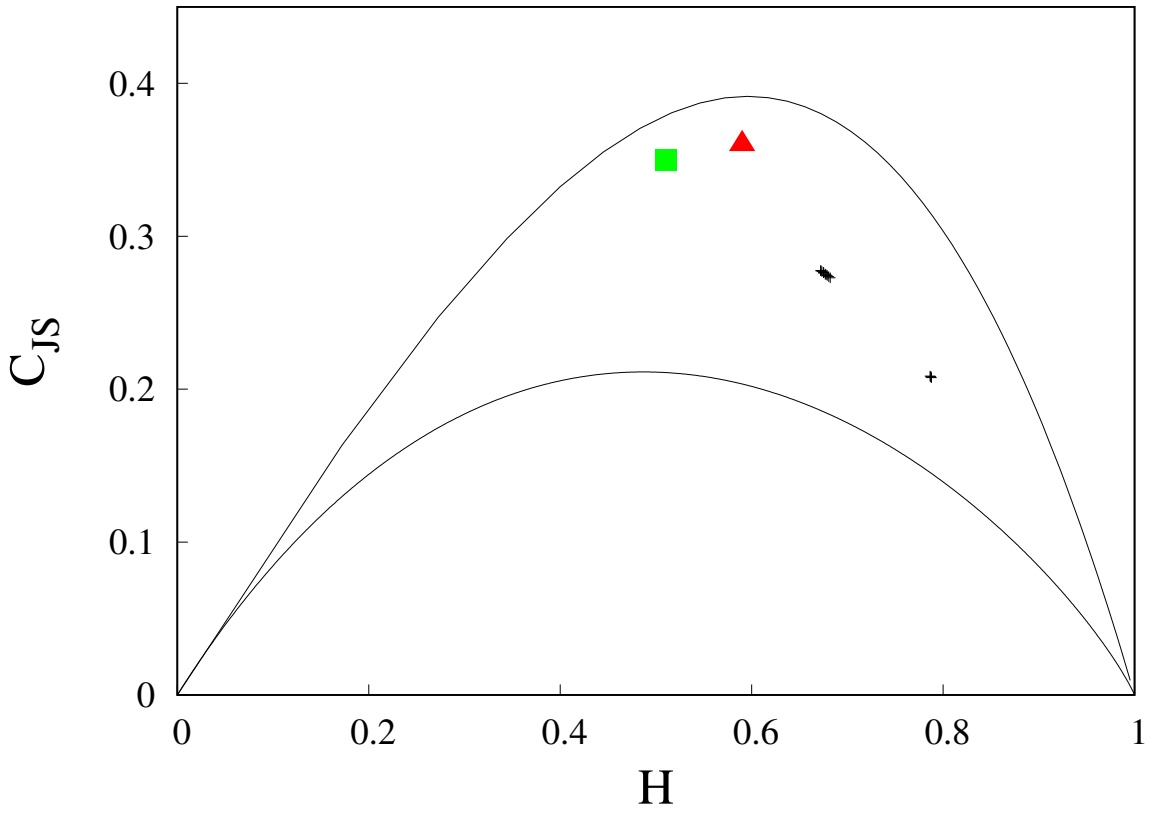

Figure 5.8. The complexity-entropy plane, showing the J-S index of the V_y velocity component in the turbulent regime (crosses) and the zonal-flow regime (plus signs).

Regarding to Figure 5.8, the J-S index for two fractals were included as a reference, whose high complexity values and intermediate entropy values were already expected, due to their high degree of structure and ordering. Thus, the J-S index for the Sierpiński carpet (7th iteration) is represented in the C-H plane by the green square. The red triangle represents a multifractal model described by Meakin (1987); Conlon et al. (2008), with a resolution of $N \times N = 2048 \times 2048$.

6 Conclusion

In summary, the significant role of turbulence in radial transport in the edge region of fusion plasmas inside tokamaks was presented, associated with the appearance of coherent structures, called zonal flows, fundamental in suppressing turbulent transport. Using a simplified model, a transition from a low confinement regime to a high confinement regime was identified. The low-confinement regime presents turbulent patterns of electrostatic potential, while the high-confinement regime is dominated by zonal flows that suppress plasma transport in the radial direction.

Overall, the study provided a detailed analysis of the L-H confinement transition, highlighting the role of zonal flows in suppressing turbulence and increasing plasma confinement. We started our analysis with two-dimensional numerical simulations of the modified Hasegawa-Wakatani equations, which provided a simplified nonlinear model for the turbulence of electrostatic resistive drift waves in plasmas.

From these simulations we obtained the spatial patterns of the electrostatic potential, where two distinct regimes were evident: the turbulent regime, characterized by vortices and associated with regions of local maxima and minima of φ; and the zonal flow regime marked by the appearance of coherent, zonally elongated structures.

The transition between both regimes was studied based on bifurcation diagrams constructed by varying the control parameter, α, related to adiabaticity. The bifurcation diagram showed that the ratio between the kinetic energy contained in the zonal modes and the total kinetic energy increases abruptly during the transition.

We showed that the J-S complexity-entropy index computed using shearlets allows to identify localized regions of lower entropy and higher complexity related to structures in a simple fractal image. After that, we applied to the poloidal component of the velocity field. In the turbulent regime, high entropy values and low complexity values are predominant, whereas in the zonal flow, the opposite is observed with low entropy values and high complexity values being found.

The bifurcation diagrams associated with the averaged normalized Shannon entropy H, and the averaged Jensen-Shannon complexity C_{JS}, show what has already been observed in previous results. For the average normalized Shannon entropy during the L-H transition, indicates that turbulent patterns exhibit higher entropy compared to the zonal flow regime. While for he average J-S complexity demonstrates a transition from lower to higher complexity values.

Reference List

Aguirre, A. (1995). Uma introdução à análise espectral de séries temporais econômicas. (081).

Allouche, J.-P. and Shallit, J. (2003). Multidimensional Automatic Sequences, página 405–427. Cambridge University Press.

Anderson, J. and Hnat, B. (2017). Statistical analysis of hasegawa-wakatani turbulence. Physics of Plasmas, 24.

Artsimovich, L. (1972). Tokamak devices. Nuclear Fusion, 12(2):215.

Badii, R. and Politi, A. (1997). Complexity: Hierarchical Structures and Scaling in Physics. Cambridge Nonlinear Science Series. Cambridge University Press.

Bianchi, M. F. d. (2006). Extração de características de imagens de faces humanas através de wavelets, PCA e IMPCA. PhD thesis, Universidade de São Paulo.

Biskamp, D. (1997). Nonlinear magnetohydrodynamics. Number 1. Cambridge University Press.

Bittencourt, J. (2013). Fundamentals of Plasma Physics. Springer New York.

Braginskii, S. I. (1965). Transport Processes in a Plasma. Reviews of Plasma Physics, 1:205.

Brazhe, A. (2018). Shearlet-based measures of entropy and complexity for two-dimensional patterns. Physical Review E, 97.

Burrell, K. H. (1994). Summary of experimental progress and suggestions for future work (h mode confinement). Plasma Physics and Controlled Fusion, 36(7A):A291.

Burrell, K. H. (1997). Effects of E×B velocity shear and magnetic shear on turbulence and transport in magnetic confinement devices. Physics of Plasmas, 4(5):1499–1518.

Camargo, S. J., Biskamp, D., and Scott, B. D. (1995). Resistive drift-wave turbulence. Physics of Plasmas, 2:48–62.

Carslaw, H. S. (1930). Theory of Fouriers series and integrals. Dover.

Chen, F. F. (2012). An Indispensable Truth: How Fusion Power Can Save the Planet. Physics Today, 65(2):51–53.

Chen, F. F. (2016). Introduction to Plasma Physics and Controlled Fusion. Springer International Publishing.

Conlon, P., Gallagher, P., McAteer, R., Ireland, J., Young, C., Kestener, P., Hewett, R., and Maguire, K. (2008). Multifractal properties of evolving active regions. Solar Physics, 248:297–309.

Conn, R. W. (2008). nuclear fusion. Encyclopedia Britannica.

Cooley, J. W. and Tukey, J. W. (1965). An algorithm for the machine calculation of complex fourier series. Mathematics of computation, 19(90):297–301.

Crepaldi, C. (2021). Busca por evidências de dinâmica caótica nas flutuações turbulentas de densidade em plasmas.

Daubechies, I. (1988). Orthonormal bases of compactly supported wavelets. Communications on pure and applied mathematics, 41(7):909–996.

Daubechies, I. (1990). The wavelet transform, time-frequency localization and signal analysis. IEEE transactions on information theory, 36(5):961–1005.

Dewhurst, J. M. (2010). Statistical description and modelling of fusion plasma edge turbulence. PhD thesis, University of Warwick.

Diamond, P., Hasegawa, A., and Mima, K. (2011). Vorticity dynamics, drift wave turbulence, and zonal flows: a look back and a look ahead. Plasma Physics and Controlled Fusion, 53(12):124001.

Diamond, P. H., Itoh, S.-I., Itoh, K., and Hahm, T. S. (2005). Zonal flows in plasma—a review. Plasma Physics and Controlled Fusion, 47(5):R35.

Diamond, P. H., Liang, Y.-M., Carreras, B. A., and Terry, P. W. (1994). Self-regulating shear flow turbulence: A paradigm for the l to h transition. Phys. Rev. Lett., 72:2565–2568.

Dolan, T. J. (2013a). Fusion Research: Principles. Elsevier.

Dolan, T. J. (2013b). Magnetic Fusion Technology, volume 19. Springer London.

Donoho, D. (2001). Sparse components of images and optimal atomic decompositions. Constructive Approximation, 17:353–382.

Duflot, L.-A., Reisenhofer, R., Tamadazte, B., Andreff, N., and Krupa, A. (2019). Wavelet and shearlet-based image representations for visual servoing. The International Journal of Robotics Research, 38(4):422–450.

Farge, M. (1992). Wavelet transforms and their applications to turbulence. Annual Review of Fluid Mechanics, 24:395–458.

Frigo, M. and Johnson, S. G. (2005). The design and implementation of FFTW3. Proceedings of the IEEE, 93(2):216–231. Special issue on "Program Generation, Optimization, and Platform Adaptation".

Frisch, U. and Kolmogorov, A. (1995). Turbulence: The Legacy of A. N. Kolmogorov. Cambridge University Press.

Gabor, D. (1946). Theory of communication. j inst electr eng–part iii. Radio Commun Eng, 93:429–457.

Gallagher, S. J. (2013). Zonal flow generation through four wave interaction in reduced models of fusion plasma turbulence. PhD thesis, University of Warwick.

Graham, A. (2002). The abc's of nuclear science. The Physics Teacher, 40(3):190–190.

Grossman, A. and Morlet, J. (1985). Decomposition of functions into wavelets of constant shape, and related transforms. Mathematics and Physics: Lectures on Recent Results, 11:135–165.

Guo, K., Kutyniok, G., and Labate, D. (2006). Sparse multidimensional representations using anisotropic dilation and shear operators. Wavelets and splines, 14:189–201.

Guosheng, X. and Xingquan, W. (2017). Understanding l–h transition in tokamak fusion plasmas. Plasma Science and Technology, 19(3):033001.

Gutierrez, C. E. (2002). Eliminação do ruído por encolhimento de wavelets–uma aplicação à série de preço spot de energia elétrica do brasil. Universidade Católica do Rio de Janeiro, Rio de Janeiro–Brasil.

Haar, A. (1909). Zur theorie der orthogonalen funktionensysteme. Georg-August-Universitat, Gottingen.

Hasegawa, A. and Mima, K. (1978). Pseudo-three-dimensional turbulence in magnetized nonuniform plasma. The Physics of Fluids, 21(1):87–92.

Hasegawa, A. and Wakatani, M. (1983). Plasma edge turbulence. Physical Review Letters, 50:682–686.

Horton, W. (1999). Drift waves and transport. Reviews of Modern Physics, 71:735–778.

Häuser, S. and Steidl, G. (2014). Fast finite shearlet transform.

Jassby, D. (1977). Tokamak devices and reactors. Technical report.

Kadomtsev, B. B. (1988). Evolution of the tokamak. Plasma Physics and Controlled Fusion, 30(14):2031.

Keilhacker, M. and Team, A. (1985). The asdex divertor tokamak. Nuclear Fusion, 25(9):1045.

Kikuchi, M., Lackner, K., Tran, M. Q., and Agency., I. A. E. (2012). Fusion physics. International Atomic Energy Agency.

Kraichnan, R. H. (1967). Inertial ranges in two-dimensional turbulence. The Physics of Fluids, 10(7):1417–1423.

Krommes, J. A. (2012). The Gyrokinetic Description of Microturbulence in Magnetized Plasmas. Annual Review of Fluid Mechanics, 44(1):175–201.

Kutyniok, G. and Labate, D. (2012). Introduction to Shearlets, páginas 1–38.

Labate, D., Lim, W.-Q., Kutyniok, G., and Weiss, G. (2005). Sparse multidimensional representation using shearlets. In Wavelets XI, volume 5914, páginas 254–262. SPIE.

Langmuir, I. (1928). Oscillations in ionized gases. Proceedings of the National Academy of Sciences, 14(8):627–637.

López-Ruiz, R., Mancini, H., and Calbet, X. (1995). A statistical measure of complexity. Physics Letters A, 209(5):321–326.

Magossi, J. C., de Abreu, P. H. C., da Costa Barros, A. C., and Paviotti, J. R. (2021). A medida de informação de shannon: Entropia. Revista Brasileira de História da Matemática, 21:45–72.

Mallat, S. G. (1989). A theory for multiresolution signal decomposition: the wavelet representation. IEEE transactions on pattern analysis and machine intelligence, 11(7):674–693.

Meakin, P. (1987). Diffusion-limited aggregation on multifractal lattices: A model for fluid-fluid displacement in porous media. Physical Review A, 36(6):2833.

Meyer, I. et al. (1992). Wavelets and applications, volume 31. Masson Paris.

Meyer, Y. (1986). Ondelettes et fonctions splines. Séminaire Équations aux dérivées partielles (Polytechnique) dit aussi" Séminaire Goulaouic-Schwartz", páginas 1–18.

Miranda, R. A., Rempel, E. L., and Chian, A.-L. (2015). On–off intermittency and amplitude-phase synchronization in keplerian shear flows. Monthly Notices of the Royal Astronomical Society, 448(1):804–813.

Miranda, R. A., Valdivia, J. A., Chian, A. C.-L., and Muñoz, P. R. (2021). Complexity of magnetic-field turbulence at reconnection exhausts in the solar wind at 1 au. The Astrophysical Journal, 923:132.

Morlet, J. (1983). Sampling theory and wave propagation. In Issues in acoustic Signal—image processing and recognition, páginas 233–261. Springer.

Najmabadi, F. and Prager, S. C. (2007). fusion reactor. Encyclopedia Britannica.

Numata, R., Ball, R., and Dewar, R. L. (2007). Bifurcation in electrostatic resistive drift wave turbulence. Physics of Plasmas, 14.

Nusse, H. E., Yorke, J. A., and Kostelich, E. J. (1994). Bifurcation Diagrams, páginas 229–268. Springer US, New York, NY.

Oppenheim, A., Willsky, A., and Nawab, S. (1997). Signals & Systems. Prentice-Hall signal processing series. Prentice-Hall International.

Powell, G. E. and Percival, I. C. (1979). A spectral entropy method for distinguishing regular and irregular motion of hamiltonian systems. Journal of Physics A: Mathematical and General, 12:2053–2071.

Press, W. H. (2007). Numerical recipes 3rd edition: The art of scientific computing. Cambridge university press.

Pushkarev, A. (2013a). Self-organization of isotopic and drift-ware turbulence. PhD thesis, Ecully, Ecole centrale de Lyon.

Pushkarev, A. (2013b). Self-organization of isotopic and drift-ware turbulence. PhD thesis. Thèse de doctorat dirigée par Bos, Wouter Mécanique Ecully, Ecole centrale de Lyon 2013.

Rempel, E. L., Chian, A. C.-L., and Miranda, R. A. (2007). Chaotic saddles at the onset of intermittent spatiotemporal chaos. Physical Review E, 76(5):056217.

Rempel, E. L., Miranda, R. A., and Chian, A. C.-L. (2009). Spatiotemporal intermittency and chaotic saddles in the regularized long-wave equation. Physics of Fluids, 21(7).

Rosso, O. A., Zunino, L., Pérez, D. G., Figliola, A., Larrondo, H. A., Garavaglia, M., Martín, M. T., and Plastino, A. (2007). Extracting features of gaussian self-similar stochastic processes via the bandt-pompe approach. Phys. Rev. E, 76:061114.

Shannon, C. E. (1948). A mathematical theory of communication. Bell System Technical Journal, 27:379–423.

Stangeby, P. C. et al. (2000). The plasma boundary of magnetic fusion devices, volume 224. Institute of Physics Pub. Philadelphia, Pennsylvania.

Torrence, C. and Compo, G. P. (1998). A practical guide to wavelet analysis. Bulletin of the American Meteorological Society, 79:61–78.

Vaidyanathan, S., Sambas, A., Azar, A. T., Rana, K., and Kumar, V. (2021). Chapter 7 - a new 4-d hyperchaotic temperature variations system with multistability and strange attractor, bifurcation analysis, its active backstepping control, and circuit realization. In Vaidyanathan, S. and Azar, A. T., editors, Backstepping Control of Nonlinear Dynamical Systems, Advances in Nonlinear Dynamics and Chaos (ANDC), páginas 139–164. Academic Press.

Vaseghi, S. (2000). Advanced Digital Signal Processing and Noise Reduction. Wiley.

Wagner, F., Becker, G., Behringer, K., Campbell, D., Eberhagen, A., Engelhardt, W., Fussmann, G., Gehre, O., Gernhardt, J., Gierke, G. v., et al. (1982). Regime of improved confinement and high beta in neutral-beam-heated divertor discharges of the asdex tokamak. Physical Review Letters, 49(19):1408.

Wakatani, M. and Hasegawa, A. (1984). A collisional drift wave description of plasma edge turbulence. The Physics of fluids, 27(3):611–618.

Wesson, J. and Campbell, D. (2004). Tokamaks. International series of monographs on physics. Clarendon Press.

Xi, H. and Gunton, J. D. (1995). Spatiotemporal chaos in a model of rayleigh-bénard convection. Phys. Rev. E, 52:4963–4975.

Zhou, P.-b. (1993). Finite Difference Method, páginas 63–94. Springer Berlin Heidelberg, Berlin, Heidelberg.